Experimental Crystallization of a High-K Arc Basalt: the Golden Pumice, Stromboli Volcano (Italy)

Ida Di Carlo, Michel Pichavant, Silvio G. Rotolo, Bruno Scaillet

Experimental Crystallization of a High-K Arc Basalt: the Golden Pumice, Stromboli Volcano (Italy)

IDA DI CARLO[1], MICHEL PICHAVANT[2,*], SILVIO G. ROTOLO[1] and BRUNO SCAILLET[2]

[1] UNIVERSITÁ DI PALERMO, DIPARTIMENTO DI CHIMICA E FISICA DELLA TERRA (CFTA) VIA ARCHIRAFI, 36, 90123 PALERMO, ITALY
[2] INSTITUT DES SCIENCES DE LA TERRE D'ORLEANS, CNRS/INSU, UMR 6113 1A RUE DE LA FEROLLERIE, ORLEANS CEDEX 2, FRANCE

ABSTRACT

The near-liquidus crystallization of a high-K basalt (PST-9 golden pumice, 49·4 wt % SiO_2, 1·85 wt % K_2O, 7·96 wt % MgO) from the present-day activity of Stromboli (Aeolian Islands, Italy) has been experimentally investigated between 1050 and 1175°C, at pressures from 50 to 400 MPa, for melt H_2O concentrations between 1·2 and 5·5 wt % and ΔNNO ranging from –0·07 to +2·32. A drop-quench device was systematically used. AuPd alloys were used as containers in most cases, resulting in an average Fe loss of 13% for the 34 charges studied. Major crystallizing phases include clinopyroxene, olivine and plagioclase. Fe–Ti oxide was encountered in a few charges. Clinopyroxene is the liquidus phase at 400 MPa down to at least 200 MPa, followed by olivine and plagioclase. The compositions of all major phases and glass vary systematically with the proportion of crystals. Ca in clinopyroxene sensitively depends on the H_2O concentration of the coexisting melt, and clinopyroxene Mg-number shows a weak negative correlation with ΔNNO. The experimental data allow the liquidus surface of PST-9 to be defined. When used in combination with melt inclusion data, a consistent set of pre-eruptive pressures (100–270 MPa), temperatures (1140–1160°C) and melt H_2O concentrations is obtained. Near-liquidus phase equilibria and clinopyroxene Ca contents require melt H_2O concentrations <2·7–3·6 and 3 ± 1 wt %, respectively, overlapping with the maximum frequency of glass inclusion data (2·5–2·7 wt % H_2O). For olivine to crystallize close to the liquidus, pressures close to 200 MPa are needed. Redox conditions around ΔNNO = +0·5 are inferred from clinopyroxene compositions. The determined pre-eruptive parameters refer to the storage region of golden pumice melts, which is located at a depth of around 7·5 km, within the metamorphic arc crust. Golden pumice melts ascending from their storage zone along an adiabat will not experience crystallization on their way to the surface.

KEY WORDS: *basalt; pumice; experiment; phase equilibria; Stromboli*

INTRODUCTION

Knowledge of the physico-chemical conditions prevailing in magmas is a prerequisite for modelling igneous systems and volcanic eruptions. Possible approaches to reach this goal include: (1) geothermometry and geobarometry on phenocryst and cumulate assemblages from quenched eruption products (e.g. Luhr & Carmichael, 1980; Ghiorso & Sack, 1991; Lindsley & Frost, 1992; Salvioli-Mariani *et al.*, 2002); (2) melt inclusion studies (e.g. Roggensack *et al.*, 1997; Metrich *et al.*, 2001; Wallace, 2005); (3) experimental simulations of crystal–liquid equilibria (e.g. Johnson *et al.*, 1994). During the past 20 years, experimental studies have increasingly been used to constrain the pre-eruptive parameters (*P*, *T*, fO_2, fS_2, fH_2O) of subvolcanic magma bodies (e.g. Rutherford *et al.*, 1985; Martel *et al.*, 1998; Scaillet & Evans,

1999; Costa *et al*., 2004). However, this approach has mainly concerned silicic to intermediate (i.e. rhyolitic–andesitic) systems, virtually excluding more mafic compositions. This situation reflects the technical difficulties associated with the experimental crystallization of mafic melts in the presence of volatiles (e.g. Sisson & Grove, 1993*a*). Added to this are problems specific to mafic magmas, including the definition of liquid compositions and the possibility of complex open-system polybaric crystallization histories (e.g. O'Hara, 1977). Despite these difficulties, there is a need to apply the experimental approach to mafic magmas, in particular to complement data from melt inclusion studies. This study details the experimental simulation of near-liquidus crystal–liquid equilibria for a high-K basaltic melt from an active volcano, Stromboli (Aeolian Islands, Italy).

VOLCANOLOGICAL AND PETROLOGICAL BACKGROUND

Stromboli, the northernmost volcano of the Aeolian archipelago, southern Italy (Fig. 1), lies on 20 km thick continental crust (Morelli *et al*., 1975). It was built during the last 200 kyr in six cycles of activity, separated from each other by caldera or flank collapses (Pasquarè *et al*., 1993). Stromboli magmas typically show a trend of K enrichment with time, from early erupted calc-alkaline, intermediate high-K calc-alkaline and shoshonites to late K-rich products, the maximum K enrichment being attained in the late K-series (13-6 ka BP). Products younger than 6 ka, including those emitted during present-day activity, are shoshonitic to high-K basalts (Francalanci *et al*., 2004). Coupled isotopic and elemental variations suggest that the parental magmas originate from a metasomatized mantle source. These magmas feed one or more crustal reservoirs in which they evolve by fractional crystallization, assimilation and mixing. These reservoirs, discontinuously refilled and tapped, provide the magmas associated with the present-day activity (Francalanci *et al*., 1989, 1993, 2004).
Stromboli is famous for its persistent activity, established 1400–1800 years ago (Rosi *et al*., 2000), which consists of intermittent low-energy explosions (3–6 events/h) throwing crystal-rich scoria, gas and ash to heights <150 m above the summit vents. This steady-state activity, reflecting the equilibrium between emissions and magma supply from below, is periodically interrupted by *major explosions* (Barberi *et al*., 1993; Speranza *et al*., 2004), which occur unpredictably 0·5–3 times/year, and consist of much higher jets than normal, resulting in fallout of meter-sized ballistic blocks and lapilli showers within a distance of several hundreds of meters from the craters upon the settled areas of Ginostra and Stromboli (Fig. 1). *Eruptive paroxysms* represent the least frequent eruptive manifestations at Stromboli (the last occurred in April 2003), but are also the most violent. They consist of fallout of bombs and lithic blocks (up to 10 tons) able to reach Ginostra and Stromboli villages, showers of scoria, tephra accumulation, glowing avalanches and tsunamis (Barberi *et al*., 1993; Metrich *et al*., 2005).
The distinctive feature of major explosions and eruptive paroxysms is the eruption of different products representing two different magmas: a highly vesicular pumice, yellowish in color (hereafter designated as golden pumice), and a black scoria. The scoria, which is volumetrically far more abundant than the pumices, contains ~50 vol. % phenocrysts (olivine, clinopyroxene, plagioclase), whereas the pumices are typically crystal-poor (~10 vol. %, e.g. Metrich *et al*., 2001). These magma types are often intermingled at the hand-specimen scale and phenocrysts from the black scoria may be found within the golden pumice.

Despite their differences in crystal content, the black scoria (BS) and golden pumice (GP) bulk-rock compositions are similar to each other (high-K shoshonitic basalt, Francalanci *et al*., 2004). Their olivine and clinopyroxene phenocrysts divide into two compositional groups. The first group consists of crystals with relatively primitive characteristics (olivines with Fo >78 and up to 91, some containing Cr-spinel inclusions; diopsidic high-Cr, low-Ti clinopyroxenes with Mg-number up to 0·9, Metrich *et al*., 2001; Bertagnini *et al*., 2003;

Francalanci *et al*., 2004). The second group includes olivines with Fo mostly between 68 and 74 and clinopyroxenes with Mg-number mostly between 0·7 and 0·8. Compositions from the first group tend to be associated with the GP and those from the second group with the BS (Metrich *et al*., 2001; Francalanci *et al*., 2004). Compositional gaps separate the two groups, suggesting that two main olivine + clinopyroxene crystallization stages are recorded in present-day Stromboli magmas. In contrast, plagioclase crystallization appears to be restricted to shallow levels (e.g. Francalanci *et al*., 2004). Plagioclase in BS shows a large range of compositions, and is complexly zoned from An_{60} to An_{88}. Calcic compositions ($An_{75–90}$) are observed in growth zones surrounding plagioclase xenocrysts inherited from the BS magma and partially reacted in the GP magma (Landi *et al*. (2004).

Important insights on magmatic volatiles are given by the study of olivine-hosted melt inclusions (MI). In golden pumices, MI have elevated volatile concentrations (1·8–3·4% H_2O, 707–1887 ppm CO_2, 610–2500 ppm S, 980–2640 ppm Cl, 641–1364 ppm F; Metrich *et al*., 2001; Bertagnini *et al*., 2003). These volatile-rich inclusions yield minimum entrapment pressures of ~350 MPa (Bertagnini *et al*., 2003), when calculated using the solubility model for H_2O–CO_2 fluid mixtures of Papale (1999). In contrast, black scoria are characterized by volatile-poor MI (e.g. H_2O ≤0·2%), suggesting trapping of an extensively degassed melt at very low pressures.

Phenocryst and MI data strongly suggest that the crystal-rich scoria represents a shallow-level, degassed, crystal mush (the resident magma). This magma feeds lava flows such as those during the 2002–2003 eruption, and normal Strombolian activity. The resident magma is periodically injected with a volatile-rich, crystal-poor, magma emitted as golden pumice during paroxysms and major explosions (e.g. Francalanci *et al*., 2004).

EXPERIMENTAL STRATEGY AND STARTING MATERIAL

Near-liquidus crystal–liquid equilibria were experimentally determined to constrain the *P*–*T*–H_2O–fO_2 conditions of the golden pumice magma. Four experimental variables are considered: pressure, temperature, melt H_2O content and fO_2. Because minimum entrapment pressures calculated from melt inclusion volatile contents cluster near 350 MPa (Bertagnini *et al*., 2003), 400 MPa was selected as the upper bound of the experimental pressure range. The lower bound was set at 50 MPa. Temperature was varied between 1050 and 1175°C. The effect of varying temperature on phase equilibria was investigated systematically at 400 MPa and that of varying pressure systematically at 1100°C. In most experiments (i.e. fixed *P*–*T*–fH_2), charges with different melt H_2O contents were run together to determine the effect of H_2O on phase equilibria. Oxygen fugacity was not systematically varied, but the experiments cover an fO_2 range larger than 2 log units.

Golden pumice sample PST-9 (Table 1) was selected as the starting material. It is the same sample as used previously in 1 atm continuous cooling experiments by Conte *et al*. (2004). PST-9 comes from a 10 cm thick layer erupted in the period AD 800–1600 (M. Pompilio, personal communication, 2001). This GP layer was found in a trench dug on the summit area of the volcano, at a height of 795 m above sea level (a.s.l.); the sample was kindly supplied by Dr M. Pompilio (Fig. 1). PST-9 is strongly vesicular (~60 vol. % vesicles) and slightly porphyritic (~11 vol. % crystals, within the range of other pumices), and its glassy groundmass is free of microlites. Modal proportions (vol. %, vesicle-free basis) are 89% glass, 8% clinopyroxene, 1–2% olivine, 1–2% plagioclase. Mass-balance calculations (Albarède, 1995) using the major element compositions of the bulk-rock and the phenocrysts (assumed

homogeneous) are in good agreement with the point counting data for glass (91%), clinopyroxene (8%) and olivine (1%). For plagioclase, a slightly negative proportion is obtained, consistent with the very low abundance of plagioclase in the pumice. Metrich *et al.* (2001) found vol. % plagioclase ≥clinopyroxene in other golden pumices, but noted that most crystals are in fact inherited from the crystal-rich resident BS magma and that golden pumice melts are nearly aphyric.

PST-9 is a K-basalt with 49·4 wt % SiO_2 and 1·85 wt % K_2O (Table 1). TiO_2 (0·79 wt %) is low, as expected for a mafic arc melt, whereas CaO and CaO/Al_2O_3 are both high (respectively 12·7 wt % and 0·81, Table 1). Although golden pumices emitted over the last few centuries are all compositionally very similar (e.g. Francalanci *et al.*, 2004), PST-9 has the highest MgO (7·96 wt %), Cr, Ni and CaO/Al_2O_3. These geochemical characteristics indicate that PST-9 is relatively primitive, although its Mg-number (0·64, calculated with FeO_t) is low for a typical primary mantle melt. Rare earth element (REE) abundances are high for such a mafic rock (La = 197 x C1). REE patterns are light REE (LREE) enriched (La_N/Yb_N = 15·3), with a slight negative Eu anomaly (Eu/Eu^* = 0·84).

Clinopyroxenes in PST-9 have Mg-number (calculated with FeO_t) mostly between 0·7 and 0·8. One analyzed microphenocryst has an Mg-number of 0·89 and 0·83 wt % Cr_2O_3 (Table 1), within the range of the diopsidic group (Francalanci *et al.*, 2004). More evolved compositions, typical of crystals inherited from the BS magma, were also found (Table 1, column 4) and correspond to xenocrysts incorporated in the GP melt during eruption. Olivines show complex zoning patterns, with rims in the range $Fo_{85–88}$ and cores in the range $Fo_{70–84}$ (Table 1). Compositions with Fo <78–80 (Table 1, column 6) probably correspond to xenocrysts (Metrich *et al.*, 2001). Scanning electron microscope (SEM) observations reveal olivine crystals crowded with melt inclusions (e.g. Metrich *et al.*, 2001; Bertagnini *et al.*, 2003), some of which have crystallized to Al-rich clinopyroxene, a K-rich phase (probably a mica) and sulphides. Plagioclase crystals often show sieve textures and thin (<15 μm) skeletal rims, and are all considered as xenocrysts derived from the crystal-rich BS magma (Landi *et al.*, 2004). They have compositions between An_{70} and An_{80}, with values up to An_{86} (Table 1). Apatite and Ti-magnetite (13–21·5 wt % TiO_2, 63·5–77 wt % FeO, 4·5–6·5 wt % Al_2O_3, 3·5–5 wt % MgO, 0·5–2·3 wt % Cr_2O_3) were found as inclusions in clinopyroxene. The glassy groundmass is homogeneous with 49·6 wt % SiO_2, 2·07 wt % K_2O, 6·41 wt % MgO and CaO/Al_2O_3 = 0·66 (Table 1).

EXPERIMENTAL METHODS

Charges and equipment

PST-9 pumice was first ground in an agate mortar to ~50 μm, then fused in air at 1400°C, 1 atm in a Pt crucible. Two cycles of melting of 2–4 h each (with grinding between them) were performed, yielding a homogeneous glass whose composition was checked by electron microprobe (Tables 1, 4 and 5). The glass was then crushed to ~10–50 μm and stored in an oven. About 30 mg of glass powder was loaded in either $Au_{90}Pd_{10}$ or $Au_{70}Pd_{30}$ capsules (15 mm length, 2·5 mm internal diameter, 0·2 mm wall thickness), depending on the experimental temperature. $Ag_{70}Pd_{30}$ tubing was also used in a few cases. Variable quantities (0·6–2 μl) of distilled water were introduced with a microsyringe at the bottom of the capsule before adding the glass powder. Capsules were sealed by arc welding, keeping them in a liquid nitrogen bath to prevent water loss. They were then put in an oven for several hours and reweighed to check for leaks.

All experiments were carried out in the same internally heated pressure vessel, working vertically and pressurized with Ar–H_2 mixtures obtained by sequential loading of H_2 and Ar at

room temperature (Scaillet *et al.*, 1992). Most experiments were performed with an initial H_2 pressure of 1 bar. Experimental fH_2 was measured using Ni–Pd–O sensors (see below). Total pressure was recorded by a transducer calibrated against a Heise Bourdon tube gauge (uncertainty ±20 bars). A double-winding molybdenum furnace was used, allowing near-isothermal conditions in the 2–3 cm long hotspot (gradient <2–3°C/cm). Temperature was measured using three thermocouples (either type S or K) and recorded continuously (uncertainty ±5°C). Overall, the run duration range was 5–25·5 h, but except for run 4 (5 h), the others lasted for an average of 18 h.

A drop-quench technique, modified after Roux & Lefevre (1992), was systematically used. Experimental capsules (up to a maximum of six) plus the fH_2 sensor capsule were placed together in a thin alumina tube that served as a sample holder. The alumina tube was hung in the furnace hotspot by a thin (0·2 mm) Pt wire. At the end of the experiment, the Pt wire was fused electrically, allowing the sample holder to fall into the cold part of the vessel. With this device, nearly isobaric quench rates of ~100°C/s were achieved. Dropping of the sample holder causes the cold bottom gas to heat, and a successful quench is indicated by a peak of several tens of bars on the pressure readout. When the quench was unsuccessful, the vessel was opened, and the experiment was restarted and run for a few additional hours before quenching was attempted again. Only runs quenched with this technique are reported in Tables 2 and 3.

At the end of the experiment, capsules were weighed to check for leaks and then opened. For each PST-9 capsule, fragments of the run product were mounted in epoxy and polished for SEM observations and electron microprobe analyses. Some capsules were also prepared for determination of their Fe concentration by electron microprobe. Glass chips from supra-liquidus charges were selected for H_2O determination by Karl-Fisher titration (KFT). The metallic pellets in the sensor capsule were recovered, mounted in epoxy and then analyzed by electron microprobe.

Control of redox conditions

Each run included a Ni–Pd–O sensor capsule, which served to determine fH_2. These consisted of two pellets of NiPd metal mixtures (each with different Ni/Pd ratio) plus NiO, placed in either a Pt or a AuPd capsule in the presence of excess H_2O (Taylor *et al.*, 1992). Analysis of the composition of the metallic phase after the experiment allows the fO_2 of the sensor system to be determined (Pownceby & O'Neill, 1994). The fH_2 of the sensor (and by inference that of the experiment, as fH_2 is identical for all capsules) is then obtained from the water dissociation equilibrium, using the fO_2 determined above, the dissociation constant of water (Robie *et al.*, 1979) and the fugacity of pure water at the experimental P and T (Ferry & Baumgartner, 1987; Holloway, 1987; Papale, 1997). Tables 2 and 3 list sensor compositions (mole fraction of Ni in the metallic phase, X_{Ni}) and the corresponding fH_2 for each experiment.

For a given experiment (i.e. constant P–T–fH_2), the fO_2 of each charge is not constant but varies along with aH_2O (or fH_2O). The latter was determined for each charge from the H_2O content of the quenched glass, using the thermodynamic model for H_2O solution in multicomponent melts of Burnham (1979). The oxygen fugacity of each charge is then calculated from the water dissociation equilibrium, using the fH_2 and fH_2O determined above, and the dissociation constant of water (Robie *et al.*, 1979). Typical uncertainty on log fO_2 is <0·25 log units (e.g. Scaillet *et al.*, 1995; Martel *et al.*, 1999; Scaillet & Evans, 1999; Costa *et al.*, 2004). In this study, fO_2 values are expressed as deviations from the NNO (nickel–nickel oxide) buffer (ΔNNO values), calculated at the P and T of interest.

ANALYTICAL METHODS

All charges were systematically examined by SEM in back-scattered electron mode to assist in the identification of the phases and to evaluate the importance of quench crystallization. Instruments from the universities of Palermo (Cambridge LEO 440) and Orléans (JEOL WINSET JSM 6400) were both used. Electron microprobe analyses of mineral and glass phases were performed with either the Cameca Camebax or the Cameca SX-50 of the joint BRGM–CNRS facility at Orléans. Analyses were carried out under an acceleration voltage of 15 kV, counting times of 10 s and a sample current of 6 nA, except for metallic sensor phases and capsules, which were analyzed under 20 kV and 20 nA. For glasses, a defocused beam of 10 μm was used, and for minerals a focused beam of 1–2 μm. Silicate minerals were used as standards. For the oxides, the relative analytical errors are 1% (SiO_2, Al_2O_3, CaO), 3% (FeO, MgO, TiO_2) and 5% (MnO, Na_2O, K_2O, P_2O_5). Phase proportions, FeO and K_2O losses were calculated for each charge using a least-squares mass-balance routine computed after Albarède (1995), using electron microprobe compositions of the starting material and phases coexisting in the charge. The regression was based on eight major oxides, excluding MnO, P_2O_5 and H_2O.

A total of six supra-liquidus, bubble-free, experimental glasses was selected for H_2O analysis by Karl-Fischer titration, using equipment and procedures identical to those described by Behrens *et al*. (1996). These glasses served to calibrate the 'by difference' method for the measurement of the H_2O content of crystal-bearing glasses (Devine *et al*., 1995). For each electron microprobe session, the difference from 100% of electron microprobe analyses was calibrated against the dissolved glass H_2O content, using the supra-liquidus glasses of known H_2O content as standards. The uncertainty in the determination of the H_2O concentration with this method ranges from ±0·5 wt % to around ±1·0 wt % depending on glass analytical totals.

EXPERIMENTAL RESULTS

For presentation purposes, the experimental results have been divided into two groups, corresponding respectively to the 400 MPa isobaric and the 1100°C isothermal sections. For each group, experimental conditions and results are detailed in Tables 2 and 3, and experimental compositions in Tables 4 and 5, respectively. In total, 16 experiments corresponding to 34 charges are reported.

Evaluation of quench crystallization and Fe loss

Stable phases encountered include clinopyroxene, olivine, plagioclase and an oxide phase, found in one charge (10-2) and possibly in another (10-1, Table 2). When present, clinopyroxene is relatively small in size (≤10–20 μm, Fig. 2a and b). It may form clusters that mimic the shape of larger crystals. Olivines are large (≥30 μm), with tabular to equant habits (Fig. 2b). Plagioclase is tabular, usually very thin (≤5 μm) and difficult to analyse by microprobe (it could not be analyzed in charge 19-3). Large plagioclase crystals (60–120 μm in length) were encountered only at 50 MPa (charge 12-3, Fig. 2c).

Despite the use of the rapid-quench device, quench phases were detected by SEM in eight charges out of the 34 reported (Tables 2 and 3). Quench crystallization is marked in SEM images by the appearance of very thin needles that heterogeneously nucleate on clinopyroxene (Fig. 2d). Quench crystallization is correlated with, and can be evaluated from, K_2O loss calculated by mass balance. This indicates that the dominant quench phase is most probably phlogopite, consistent with its abundance in preliminary experiments performed with

relatively slow quench rates. In charges 16-7, 16-6, 15-1, 15-3 and 19-4, all with quench phases detected by SEM (Fig. 2d; Tables 2 and 3), K_2O losses are small (i.e. <10% relative), indicating no significant influence of quench crystallization on phase compositions. The highest K_2O losses were found in run 7. K_2O loss is up to 36% relative in charge 7-1, decreasing regularly with the melt H_2O content from charge 7-1 to 7-3, no quench phase being found in charge 7-4 (Table 2). Charges 7-1 and 7-2 are the only ones for which quench crystallization has a detectable influence on glass composition. Fe–Mg crystal–liquid exchange coefficients (K_d) in charges from run 7 and in those quenched without apparent problems (Tables 2 and 3) are in the same range. Overall, this indicates that quench crystallization has a minor influence in this study.

The importance of Fe loss was evaluated from the mass-balance calculations (Tables 2 and 3). FeO loss is 13% on average. Half of the charges have Fe losses ≤10% relative, six have Fe losses >20% and one has >25% loss. In general, the smallest Fe losses are associated with $Au_{90}Pd_{10}$ and the highest with $Au_{70}Pd_{30}$ capsules. However, fO_2 also has a detectable influence, Fe losses becoming higher for lower ΔNNO. Fe losses in the same range as in this study were found previously with AuPd alloys (Kawamoto & Hirose, 1994; Gaetani & Grove, 1998; Pichavant *et al*., 2002*b*), and this confirms that Fe loss can be minimized, but not suppressed, with AuPd tubing. Fe losses in $Ag_{70}Pd_{30}$ capsules (charges 19-3 and 21-4, Tables 2 and 3) are similar to those in AuPd capsules for the same experimental conditions (charges 19-2 and 3-1, Tables 2 and 3). Pre-saturating the capsules with Fe was not attempted in this study because fO_2 varies between charges for a given experiment (fH_2 is the buffered parameter, not fO_2). In addition, pre-calculating the fO_2 of a given charge is difficult, as this depends on the melt H_2O content, a variable that does not relate directly to the amount of water loaded in the capsule when crystals are present. Therefore, capsule Fe pre-saturation was considered impractical. As a substitute, some experiments were performed with FeO-enriched starting mixtures (i.e. PST-9 glass + about 10% FeO) to test for the influence of variable bulk FeO (run 14, Table 2). Results are consistent with other charges at 1150°C, 400 MPa (charges 3–1 and 21–4, the latter run with $Ag_{70}Pd_{30}$ tubing) in terms of phase assemblages and location of the saturation curves.

Evaluation of equilibrium

All the experiments from this study are of the crystallization type and attainment of equilibrium has not been tested from reversals. Nevertheless, several lines of evidence can be used to evaluate the approach to equilibrium.

(1) Experimental durations (18 h on average, except for one run of 5 h) are in the range of previous phase equilibrium studies on hydrous basalts (Sisson & Grove, 1993*b*; Barclay & Carmichael, 2004). Baker & Eggler (1987) found that 24 h was sufficient for phase assemblage and melt composition to reach a steady state at 1060°C, 1 atm for a mafic andesite composition. Bartels *et al*. (1991) obtained reproducible phase assemblages and proportions after 6 h in near-liquidus anhydrous experiments on a partially crystalline high-alumina basalt at 1280°C, 1·2 GPa. Because crystallization kinetics are dramatically faster in the presence of H_2O (quench crystallization is most important in charges that are the most H_2O-rich, e.g. charges 7-1 and 7-2), experimental durations, as used in this study, were such that equilibrium proportions of crystals/phase assemblages should have been obtained.

(2) Crystal morphologies (euhedral, equant or tabular) suggest growth at small degrees of undercooling (e.g. Muncill & Lasaga, 1987). The distribution of crystals in the charges is homogeneous and no crystal settling was recognized (Fig. 2). The difficulties encountered in

quenching the charges (see above) can be taken as indications of easy crystal nucleation and growth in our experiments.

(3) Crystals and glass phases are broadly chemically homogeneous for a given charge. Electron microprobe analyses for hydrous glasses, olivines and plagioclases have standard deviations in the same range as or lower than analytical dispersions (Tables 4 and 5), suggesting homogeneous compositions. For clinopyroxene, some chemical heterogeneity, mainly related to core–rim zonation, is apparent in some SEM images. Standard deviations of clinopyroxene analyses for a given charge may exceed 1% (i.e. higher than the analytical dispersion) for Al_2O_3 and more rarely for SiO_2, FeO, MgO and CaO (e.g. charges 7–1, 12–3 and 16–7, Tables 4 and 5). Chemical dispersions of the same type and magnitude as in this study for clinopyroxene have been found in other phase equilibrium studies of hydrous basalts (e.g. Sisson & Grove, 1993*a*, 1993*b*).

(4) Crystal–liquid exchange coefficients (K_d) calculated from the experimental data for olivine, clinopyroxene and plagioclase are in agreement with values from the literature under comparable conditions (see below for details).

(5) Sums of residuals from the mass-balance calculations range from values <1 to >5 and strongly correlate with Fe loss (Tables 2 and 3). Charges with Fe losses <10% relative have ΣR^2 <1 (0·83 on average) and a constant bulk silicate composition has been essentially maintained in those experiments. In contrast, charges with Fe losses exceeding 20% have ΣR^2 >4.

(6) Electron microprobe traverses performed on one $Au_{70}Pd_{30}$ capsule from run 5 (Table 2) yielded relatively low Fe concentrations in the metal (0·1–0·3 wt % Fe), with the highest values being found near the inner rim of the capsule. This, together with the fact that charges run with FeO-enriched starting mixtures have Fe losses in the same range as the others, suggests that the experimental capsules are not fully saturated with respect to Fe.

To summarize, a state of partial equilibrium (and not bulk equilibrium, as the capsules are not saturated with Fe) is approached in the charges as shown by the textural–morphological features and the compositional data for crystals and glasses, despite the slight chemical heterogeneity noted for clinopyroxenes. Differential Fe loss caused some dispersion in the bulk silicate composition. Nevertheless, this dispersion does not significantly affect our results: the different charges run at 1150°C, 400 MPa (runs 3, 14 and 21) and 1100°C, 200 MPa (runs 15 and 19) yield phase assemblages and saturation curves that are mutually consistent despite variable Fe losses (Tables 2 and 3). We, therefore, conclude that our experiments have reached a state of equilibrium sufficient to discuss the crystallization of Stromboli magmas.

400 MPa isobaric phase equilibria

A total of 20 charges were run at 400 MPa, covering the temperature range 1050–1175°C at 25°C intervals. Their H_2O contents range between 2·2 and 5·5 wt % and they have ΔNNO values between –0·07 and +2·32. The 400 MPa phase equilibria are represented in the *T*–melt H_2O content diagram of Fig. 3. The H_2O saturation curve is constructed after Burnham (1979). Mineral saturation curves are drawn from the experimental data in Table 2. The two charges run with the FeO-added starting mixture (14-1 and 14-2) are reported in Table 2, but they are not used in the construction of the phase diagram because their bulk composition differs strongly from PST-9. Clinopyroxene is the first phase to appear on the liquidus,

followed by olivine and then plagioclase upon lowering either *T* or melt H_2O content. At 1150°C, the liquidus is encountered for a melt H_2O content of about 3·3 wt %, and at 1100°C for about 4·3 wt % H_2O. Saturation curves have negative slopes in *T*–melt H_2O space, as expected for anhydrous phases. They are progressively steeper in the order plagioclase > clinopyroxene > olivine, but the clinopyroxene saturation curve is poorly defined for H_2O in melt >5 wt %. The diagram is characterized by a large primary clinopyroxene stability field in the high-*T*, low-melt H_2O content region. Plagioclase is restricted to the low-*T*, low-melt H_2O portion. At 1100°C, cotectic olivine + clinopyroxene crystallization occurs for melt H_2O contents ≤3·5 wt %. For olivine to crystallize at temperatures above 1100°C, melt H_2O contents <3 wt % would be required at 400 MPa. It should be noted that an oxide phase, too small to be analyzed by electron microprobe, is present in charge 10-2 at 1100°C. Because this oxide could not be analyzed, it was not included in the mass-balance calculations for that charge. As, a consequence, the calculations reveal a TiO_2 loss of 10% relative, suggesting that the missing phase is an Fe–Ti oxide. In charge 10-1, no oxide was detected by SEM but mass-balance calculations also reveal a TiO_2 loss of about 10% relative, which indicates that Fe–Ti oxide crystallization also probably occurred.

Crystallinities range between zero (supra-liquidus charges) and 53 wt % (Table 2). Clinopyroxene is by far the most abundant mineral phase, followed by plagioclase and olivine in decreasing abundance. The proportion of clinopyroxene reaches a maximum of 40 wt %, that of plagioclase 13 wt % and that of olivine 4 wt %. Both plagioclase and olivine crystallize in relatively constant amounts. Clinopyroxene:olivine weight ratios range between 6 and 13, increasing with progressive crystallization, and clinopyroxene:plagioclase ratios are around 3 (data in Table 2). Crystallization is marked mainly by an increase in the proportion of clinopyroxene at the expense of melt.

1100°C isothermal phase equilibria

At 1100°C, four pressures in addition to 400 MPa were investigated: 300, 200, 100 and 50 MPa, corresponding to a total of 14 charges (Table 3). They cover a range of melt H_2O contents between 1·2 and 4·9 wt % and ΔNNO values between +0·22 and 1·85. The 1100°C phase equilibria are portrayed in the *P*–melt H_2O content diagram of Fig. 4, where the H_2O saturation curve is from Burnham (1979). Mineral saturation curves are constructed from the data in Table 3, and from Table 2 for 400 MPa. Clinopyroxene is the liquidus phase for the three highest pressures investigated (400, 300, 200 MPa). With progressive crystallization (i.e. upon lowering melt H_2O content under isobaric conditions), clinopyroxene is joined by olivine and then plagioclase. One critical aspect of the diagram is the positive slope of the clinopyroxene saturation curve (Fig. 4). In comparison, the slopes of the saturation curves for olivine and plagioclase are nearly vertical or slightly negative. This results in the shrinkage of the clinopyroxene primary field and in the reduction of the crystallization interval with decreasing pressure. At 200 MPa, the cotectic olivine + clinopyroxene assemblage is close to the liquidus. The available experimental data suggest that the clinopyroxene and olivine saturation curves may cross below 200 MPa, as drawn in Fig. 4. Thus, olivine could replace clinopyroxene on the liquidus from ~150 MPa down to the saturation pressure for 3·5 wt % H_2O in the melt (about 100 MPa, Fig. 4). Plagioclase crystallization is restricted to melt H_2O contents <2·5 wt %. Only four-phase assemblages (clinopyroxene + olivine + plagioclase + L) were found at 50 MPa.

As expected from the change in phase relations, there are substantial variations in crystallinities with pressure. For charges having similar melt H_2O contents, crystallinities slightly decrease with decreasing pressure (e.g. from 53 wt % at 400 MPa to 31 wt % at 50

MPa, charges 10-2 and 12-1, Tables 2 and 3). Clinopyroxene becomes less abundant at lower pressures whereas olivine and plagioclase become more abundant. At 100 and 50 MPa, clinopyroxene:olivine and clinopyroxene:plagioclase weight ratios are 3–5 and 1·5–3 (respectively 6–13 and 3 at 400 MPa).

Experimental compositions

Experimental compositions are reported in full (Tables 4 and 5) for all charges in Tables 2 and 3, but compositions from charges 14-1 and 14-2 (FeO-added experiments) are excluded from the following discussion as their bulk composition differs strongly from PST-9. Clinopyroxenes are diopsides to augites with Wo contents ranging between 42 and 49%, Fs between 4 and 15% and En between 41 and 47% (Tables 4 and 5). They have low TiO_2 (0·27–0·86 wt %), and variable and relatively elevated Al_2O_3 (2·54–8·52 wt %) and Cr_2O_3 (0·04–0·70 wt %). Mg-number (calculated with FeO_t) is in the range 0·75–0·88. The average clinopyroxene–liquid exchange coefficient ($K_{d\ cpx-liq}^{Fe-Mg}$) is 0·31 ± 0·06 when calculated with FeO = FeO_t, and 0·35 ± 0·07 when calculated with FeO. In this latter case, the clinopyroxene FeO is determined from the structural formulae and the glass FeO from the expression of Kress & Carmichael (1991), using the data in Tables 2–5. These average K_d values are similar to those found in recent experimental studies of hydrous basaltic compositions at P <500 MPa (0·23–0·27, Sisson & Grove, 1993*a*; 0·28, Pichavant *et al*., 2002*a*). It should be noted that all clinopyroxene-bearing charges from Tables 2 and 3 have been averaged, with the exception of charges 14–1 and 14–2 (FeO-added experiments). Charges the most affected by either Fe loss (5–3) or quench crystallization (7–1, 7–2) have K_d values that do not significantly depart from the others (Tables 2 and 3).

Clinopyroxene crystallizes from a range of melt compositions and coexists with different mineral phases. Therefore, it is necessary to identify bulk chemical effects on clinopyroxene composition before the influence of experimental variables can be extracted. Clinopyroxene SiO_2, Al_2O_3, Mg-number, TiO_2 and Cr_2O_3 are strongly correlated with the melt fraction, determined from the mass-balance calculations. In high melt fraction charges, clinopyroxenes have high SiO_2, Cr_2O_3 and Mg-number (and En), and low Al_2O_3 and TiO_2. With advancing crystallization, they become progressively more Al_2O_3-, TiO_2- and Fs-rich, and their Mg-number (and En) decreases (Fig. 5a and b), consistent with the chemical evolution of the coexisting melt (Fig. 6a). Clinopyroxenes with the most primitive characteristics (i.e. high SiO_2, Cr_2O_3 and Mg-number) are found in charges close to the liquidus at 1100°C, 300 MPa (16–6, 16–7), 200 MPa (15–1, 15–3) and 100 MPa (9–1, Tables 3 and 5). The most evolved (i.e. with high Al_2O_3, TiO_2 and FeO_t) are from the most crystallized charges at 1050–1100°C, 400 MPa (10–2, 11–4, 11–7) and at 1100°C, 50 MPa (12–1, 12–2, Tables 2–5). FeO loss leads to an increase of clinopyroxene Mg-number but does not affect the Mg-number vs melt fraction trend, which is well defined from charges with minimal FeO losses. Chemical zonation in clinopyroxene, with MgO-rich cores and Al_2O_3- and FeO- rich rims, reproduces, at the scale of the charge, the chemical evolution between high and low melt fraction charges. Overall, the clinopyroxene composition is a sensitive indicator of the degree of crystallization of the melt.

The atomic concentration of Ca (and the Wo content) in clinopyroxene appears to be strongly correlated with $a H_2O$ or H_2O content of the melt (Fig. 7). Clinopyroxenes have atomic Ca concentration decreasing with $a H_2O$ (see also Gaetani *et al*., 1993), from 0·948 to 0·71. In detail, different trends can be distinguished, depending on the phase assemblage. The clinopyroxene + olivine trend is slightly offset toward higher Ca in comparison with the clinopyroxene trend, and the clinopyroxene + olivine + plagioclase trend is displaced toward

lower Ca contents. This indicates that compositional factors, in addition to aH_2O, also control clinopyroxene atomic Ca concentrations. Subdividing the data in Fig. 7 as a function of different temperatures or pressures does not reveal any significant effects of these parameters on the Ca content of clinopyroxene.

The effect of fO_2 on clinopyroxene composition was investigated from plots of clinopyroxene Mg-number against ΔNNO. When examined on a run-by-run basis (i.e. selecting runs 6, 7, 10, 12 and 19, where clinopyroxene occurs over a substantial fO_2 range, Tables 2 and 3), clinopyroxene Mg-number (calculated with FeO_t) is correlated positively with fO_2, and trends with similar slopes are observed between runs. However, although systematic, such trends probably cannot be attributed to the effect of fO_2 alone. This is because, in a given run, fO_2 variations between charges are obtained by changing the melt H_2O content, which also affects the melt fraction and the melt composition. Thus, variations in fO_2 are in fact coupled with variations in melt fraction. Therefore, to analyze the effect of fO_2 on clinopyroxene composition, charges from different runs (i.e. different fH_2) but with the same range of crystallinities need to be considered. The analysis was applied to high melt fraction (<10% crystals) near-liquidus charges. A total of eight charges fulfil this criterion, one at 1175°C (4-3, Table 2) and seven at 1100°C (6-1, 15-1, 15-3, 16-6, 16-7, 19-4 and 9-1, Tables 2 and 3). Fe losses are <10% except in charges 4-3 and 6-1. Clinopyroxene Mg-number ranges between 0·83 and 0·88 without any clear dependence on fO_2 in the limited ΔNNO range (from +0·41 to +1·7) covered. However, if Mg-number is calculated with FeO instead of FeO_t, a correlation emerges, clinopyroxene Mg-number (from 0·88 to 0·92) being slightly negatively correlated with ΔNNO (Fig. 8). In these near-liquidus charges, clinopyroxene Mg-number is not significantly affected by the presence of olivine (compare charges 16-7 and 16-6, Tables 3 and 5).

Olivines have Fo ranging between 74·7 and 87·3 (Tables 4 and 5). The CaO content is relatively high (average 0·32 wt %, total range 0·22–0·63 wt %) and positively correlated with MnO (average 0·27 wt %, total range 0·13–0·39 wt %). The average olivine–liquid exchange coefficient ($K_{d\ ol–liq}^{Fe–Mg}$) is 0·26 ± 0·04 when calculated with FeO = FeO_t, and 0·36 ± 0·04 when calculated with FeO, the glass FeO being determined as above. These average K_d values are close to those found in recent experimental studies of hydrous basaltic compositions at P <500 MPa (0·28–0·33, Sisson & Grove, 1993*a*; 0·33, Pichavant *et al*., 2002*a*; 0·28, Barclay & Carmichael, 2004). As for clinopyroxene, all olivine-bearing charges from Tables 2 and 3 have been averaged; the charges most affected by either FeO loss or quench crystallization do not yield anomalous values (Tables 2 and 3).

Olivine composition systematically varies with the degree of crystallization and the composition of the coexisting melt (Fig. 6b). Olivines with the highest Fo are from high melt fraction charges at 100 and 200 MPa (9-1 and 15-1, Tables 3 and 5). Those with the lowest Fo come from the most crystallized charges at 400 MPa, 1050°C (11-4 and 11-7, Tables 2 and 4). When plotted as a function of pressure, Fo contents define a bell-shaped curve with maxima at 100 and 200 MPa (Fig. 9). This is consistent with the change in phase relations with pressure noted earlier, and with the fact that, between 100 and 200 MPa, olivine crystallizes close to the liquidus (Fig. 4) with clinopyroxene. When olivine crystallizes much later than clinopyroxene (e.g. at 400 MPa, Fig. 3), Fo contents are limited to values <84. Olivines coexisting with plagioclase are the least Fo-rich, because plagioclase is restricted to charges with low melt fractions.

Plagioclase has An contents between 65·9 and 81·6, Or between 1·4 and 4·9, and an average Fe concentration of 1·26 wt % FeO (Tables 4 and 5). The plagioclase–liquid Ca–Na exchange

coefficient ($K_{d\ plg-liq}^{Ca-Na}$) ranges between 1·6 and 2·5, in good agreement with values for hydrous basaltic compositions with comparable melt H_2O contents (Sisson & Grove, 1993*a*). Plagioclase composition is primarily controlled by the degree of crystallization. When the proportion of crystals increases, An progressively decreases and Or increases. Plagioclase An content correlates negatively with pressure, the highest values being found in charges 12-3 (50 MPa) and 18-1 (100 MPa) at 1100°C (Tables 3 and 5). The lowest An contents are from the most crystallized charges at 400 MPa, 1050–1100°C (11-4, 11-7 and 10-2, Tables 2 and 4).

Compositions of experimental glasses can be discussed using CaO/Al_2O_3 as a differentiation index. Glass CaO/Al_2O_3 systematically decreases with decreasing melt fraction, reflecting the dominant influence of clinopyroxene on the liquid line of descent. Glasses have SiO_2, Al_2O_3, Na_2O, K_2O and TiO_2 progressively increasing, and CaO, FeO_t, MgO and Mg-number progressively decreasing with differentiation (Fig. 10). The most differentiated glasses occur in the 1050°C, 400 MPa crystal-rich charges where SiO_2 and K_2O reach values up to 54·3 wt % and 3·4 wt %, respectively, within the shoshonite field (Peccerillo & Taylor, 1976). Mg-number drops from 0·64 to 0·44 (charge 11-4, 7·45% FeO_t, 3·34% MgO; Table 4). The rate of decrease of Mg-number with CaO/Al_2O_3 depends on the phase assemblage, being progressively higher in the order clinopyroxene > clinopyroxene + olivine > clinopyroxene + olivine + plagioclase.

DISCUSSION

Phase assemblages and crystallization sequence of Stromboli golden pumice

Only clinopyroxene, olivine and plagioclase have been found as major crystallizing phases in our experiments on hydrous golden pumice melt, corresponding to three types of phase assemblages: clinopyroxene, clinopyroxene + olivine and clinopyroxene + olivine + plagioclase. Clinopyroxene-absent assemblages (i.e. olivine, plagioclase, olivine + plagioclase) have not been encountered, although the data suggest the possibility that olivine crystallizes alone on the liquidus at 1100°C between 150 and 100 MPa (Fig. 4). In the 1 atm continuous cooling experiments of Conte *et al*. (2004), olivine was found as the sole crystallizing phase between 1175 and 1150°C, and pigeonite appeared together with clinopyroxene and plagioclase from 1150 down to 1100°C. In our experiments, an Fe–Ti oxide phase is present in one (10-2) and probably two (10-1) subliquidus charges that are among the most oxidized (ΔNNO >1·5, Table 2). Both charges 10-2 and 10-1 have >10% crystals (10-2 with 53 wt % crystals is one of the two most crystallized charges), thus Fe–Ti oxide was not encountered at near-liquidus conditions. This suggests that, for ΔNNO <1·5, Fe–Ti oxide is late in the crystallization sequence and follows clinopyroxene, olivine and plagioclase. It is also worth noting here that phlogopite has not been found as a stable phase in this study.

One critical result of the experiments concerns the fact that clinopyroxene precedes olivine in the crystallization sequence for all the P–T–H_2O–fO_2 conditions investigated in this study. Clinopyroxene persists as the liquidus phase down to at least 200 MPa; that is, in a pressure range that is unexpectedly low on the basis of previous experimental studies on basalts (e.g. Gust & Perfit, 1987; Falloon *et al*., 1999; Pichavant *et al*., 2002*b*). Clinopyroxene (and also orthopyroxene for primary melts from lherzolitic mantle) is expected to saturate at relatively high pressures on the liquidus of basalts. Olivine would saturate at lower pressures, and multiple saturation points are expected in the range 1–1·2 GPa or above if the system is hydrous (e.g. Pichavant *et al*., 2002*b*). In the case of PST-9, co-saturation of olivine and clinopyroxene on the liquidus is possible on the basis of the available data (Fig. 4), but only at very low pressures ($P \leq$150 MPa at 1100°C). Orthopyroxene is totally absent. These features

are unusual for a relatively primitive basaltic composition (e.g. 8 wt % MgO in PST-9), but seem typical of ultra-calcic (i.e. ankaramitic) magmas from arc settings. In a recent study, Médard *et al.* (2004) established that a model nepheline-normative ultra-calcic melt, representative of those found in arc settings, is saturated at 200 MPa on its liquidus with clinopyroxene and olivine. Plagioclase was the third phase to crystallize and orthopyroxene was not encountered (Médard *et al.*, 2004). Thus, the phase relations of PST-9 are similar in several critical aspects to the ultra-calcic melt studied by Médard *et al.* (2004). Indeed, Stromboli is one of the localities where ultra-calcic melt inclusions have been recognized (Schiano *et al.*, 2000).

Another important aspect of the PST-9 crystallization sequence concerns plagioclase. Plagioclase is the third phase to appear in the sequence, whatever the pressure, between 50 and 400 MPa. Crystallization of plagioclase was observed for melt fractions between 32 and 53 wt %, irrespective of pressure, i.e. once a minimum of 30% clinopyroxene plus olivine has already crystallized. This range of crystallinities is much higher than the crystal content of the golden pumices (~10 vol. %, Metrich *et al.*, 2001). Thus, plagioclase is unlikely to saturate at an early stage in the golden pumice melts, and probably has a negligible importance in the early stages of magmatic differentiation. Golden pumice melts are undersaturated with respect to plagioclase and, therefore, are expected to dissolve plagioclase during their initial stages of interaction and mixing with the resident magma, in agreement with textures observed for plagioclase xenocrysts partially reacted in the golden pumice melt (Landi *et al.*, 2004). It should be noted that this conclusion leaves aside the small Eu anomaly found in PST-9 and other pumices (see above and Metrich *et al.*, 2001). One possibility is that this anomaly is a geochemical feature transferred from the scoria to golden pumice magmas because of magma mixing and advection of crystals. Alternatively, we cannot totally exclude the possibility that the Eu anomaly observed reflects a stage of plagioclase fractionation under *P–T*–volatile conditions that have not yet been investigated experimentally.

Pre-eruptive pressure–temperature–melt H_2O contents of the Stromboli golden pumice magma

As the golden pumice is crystal-poor, it essentially represents a magmatic liquid and thus constraints on pre-eruptive magmatic conditions can be obtained from the experimental liquidus and its dependence on pressure, temperature and aH_2O (or melt H_2O content). Because, in this study, no significant effect of fO_2 on phase equilibria was found between ~NNO and ~NNO + 2, it will be assumed in the following discussion that fO_2 changes in this ΔNNO range do not influence the location of the liquidus. The liquidus surface of PST-9 is represented in Fig. 11 for pressures <500 MPa and temperatures <1200°C. It is defined by clinopyroxene saturation curves for constant aH_2O; these are interpolated from the available experimental data. In addition to experiments from this study (Tables 2 and 3), two additional clinopyroxene saturation brackets at 1150°C, 200 MPa and 1150°C, 100 MPa, obtained with aH_2O controlled by H_2O–CO_2 fluid mixtures (Di Carlo *et al.*, in preparation), are included to locate more precisely the clinopyroxene saturation curves in the high-*T*, low-*P* part of the diagram (Fig. 11). The constant aH_2O liquidus curves all have negative slopes, becoming progressively steeper with decreasing aH_2O. To facilitate the discussion, melt H_2O concentrations have been calculated along these curves, with PST-9 taken as the melt composition and using the model of Burnham (1979). Contours of melt H_2O concentrations on the liquidus surface are shown in Fig. 11.

Assuming that PST-9 is a near-liquidus magma, one parameter among the three parameters *P*, *T* and melt H_2O content can be determined if the two others are known. Below, two types of

external constraints derived from melt inclusion studies are used: H_2O concentrations in glasses and homogenization temperatures (T_h, Metrich *et al*., 2001; Bertagnini *et al*., 2003). Glass inclusions in golden pumice olivines have H_2O concentrations ranging between 1·8 and 3·4 wt % with a well-defined frequency maximum at 2·5–2·7 wt % (n = 28; Metrich *et al*., 2001; Bertagnini *et al*., 2003). T_h values obtained from optical thermometry measurements on melt inclusions in olivine range from 1125–1140°C for golden pumices to 1101–1125°C for black scoria (Metrich *et al*., 2001). It should be noted that the homogenized glass inclusions are on average more evolved than PST-9 (i.e. those yielding the highest T_h have MgO between 6·03 and 7·88 wt %, Metrich *et al*., 2001). In addition, T_h values represent temperatures of melt entrapment by growing phenocrysts. Therefore, 1140°C is a minimum value for the liquidus temperature of golden pumice melt. At 1140°C, and for melt H_2O contents between 2·5 and 2·7 wt % (Fig. 11), the liquidus surface is intersected between 100 and 190 MPa. Keeping the range of melt H_2O contents unchanged, but taking a liquidus temperature of 1160°C instead of 1140°C, higher pressures, between 220 and 270 MPa, are obtained on the liquidus surface (Fig. 11). Varying the H_2O concentration of the melt on either side of the 2·5–2·7 wt % H_2O maximum would alternatively increase or decrease these conditions towards higher or lower pressures. On average, pressures >100 MPa and up to 270 MPa on the liquidus surface are suggested for 1140–1160°C.

Clinopyroxenes in the golden pumice include a compositionally distinctive group of high-Cr, high-Mg-number and low-Ti, low-Al diopsidic phenocrysts and microphenocrysts. Experimental clinopyroxenes with these characteristics were obtained in several charges over a range of conditions, especially pressure, but also melt H_2O concentration and ΔNNO (charges 9-1, 15-1, 15-3, 19-4, 16-6 and 16-7). It is worth stressing that these clinopyroxene compositions are obtained experimentally only when the proportions of crystals are small (<10%). This strongly suggests that diopsidic clinopyroxene phenocrysts represent near-liquidus crystallization products of the golden pumice melts. At 1100°C, high-Cr, high-Mg-number and low-Ti, low-Al clinopyroxenes are found at 300 MPa for melt H_2O concentrations between 3·5 and 4·0 wt %, at 200 MPa for melt H_2O concentrations between 2·7 and 3·6 wt %, and at 100 MPa for melt H_2O concentrations around 2·6 wt %. These melt H_2O contents are maxima for such clinopyroxene to be present at temperatures >1100°C (possibly up to $\geq$ 1140°C) near the liquidus. At 200 MPa, the range of melt H_2O contents constrained by near-liquidus clinopyroxene crystallization would thus be <2·7–3·6 wt %, overlapping with the average glass inclusion H_2O concentrations (2·5–2·7 wt %). The diopsidic clinopyroxene phenocrysts and microphenocrysts are highly calcic, with Ca concentrations up to 0·91 c.p.f.u., and this is consistent with crystallization from melts having H_2O concentrations of 3 ± 1 wt %, or with $a$$H_2O$ of about 0·45 (Fig. 7). Therefore, conditions of near-liquidus clinopyroxene crystallization and its Ca content suggest a range of H_2O concentrations in the golden pumice melts in agreement with the data from glass inclusions.

Additional constraints are provided by olivine saturation. As for clinopyroxene, olivine saturation curves for constant $a$$H_2O$ have been constructed by interpolating the experimental olivine saturation brackets available at 400 MPa (1100, 1075°C) and 1100°C (300, 200 MPa, Tables 2 and 3; Figs 3 and 4). Olivine saturation curves for $a$$H_2O$ = 0·3–0·6 are reasonably well defined in the range 1075–1100°C and 200–400 MPa. As no olivine was found in the two experiments performed with H_2O–CO_2 mixtures at 1150°C, 100 and 200 MPa (Di Carlo *et al*., in preparation), olivine saturation curves cannot be drawn very far above 1100°C (Fig. 11). Compared with clinopyroxene, the olivine saturation curves are distinctly flatter (for clarity, only the $a$$H_2O$ = 0·5 curve is shown; Fig. 11). For $a$$H_2O$ = 0·5, temperatures along the olivine saturation curve are lower than along the clinopyroxene saturation curve at a given pressure,

which reflects the respective order of crystallization of these two phases, as discussed above. However, the clinopyroxene and olivine $aH_2O = 0{\cdot}5$ saturation curves are within 10–20°C of each other at 200 MPa. At this pressure, olivine would be a near-liquidus phase, a requirement for trapping primitive melts as inclusions and for crystallizing Fo-rich olivines (Metrich *et al.*, 2001; Bertagnini *et al.*, 2003; Fig. 9). T_h values in pumices (1125–1140°C; see above) are in good agreement with temperatures along the $aH_2O = 0{\cdot}5$ olivine saturation curve for pressures around 200 MPa (Fig. 11). The highest T_h values are for melt inclusions hosted in Fo_{88}; that is, close to the most Fo-rich olivines crystallized in this study ($Fo_{87{\cdot}3}$).

The two olivine-bearing charges at 1100°C, 200 MPa (15-1 and 15-3, Table 3) have melt H_2O concentrations of 2·7 and 3·1 wt %, a maximum for olivine to be present near the liquidus at >1100°C (i.e. at 1120–1130°C along the olivine saturation curve; Fig. 11). Olivines in these two charges have Fo contents of 87·3 and 86·2 (Tables 3 and 5). In comparison, crystals in equilibrium with the golden pumice range between Fo_{83} and Fo_{87} (Bertagnini *et al.*, 2003). Olivines whose glass inclusion H_2O concentrations have been measured have Fo contents between 81 and 88, with a frequency maximum at $Fo_{83–84}$ (Metrich *et al.*, 2001; Bertagnini *et al.*, 2003). Therefore, golden pumice olivine compositions are well reproduced experimentally, although the temperature of 1100°C is slightly too low. The rare crystals with Fo as high as 91 (e.g. Bertagnini *et al.*, 2003) are interpreted as xenocrysts (e.g. Marsh, 1996; Danyushevsky *et al.*, 2002; Di Carlo *et al.*, in preparation).

To summarize, the status of PST-9 as a near-liquidus magma, combined with H_2O concentrations and homogenization temperatures from glass inclusion studies, allows a set of liquidus *P*–*T*–melt H_2O concentration values (1140–1160°C, 100–270 MPa, 2·5–2·7 wt % H_2O in melt) to be determined. Near-liquidus clinopyroxene crystallization and compositions require melt H_2O concentrations either <2·7–3·6 or 3 ± 1 wt %, compatible with the maximum frequency of glass inclusion H_2O concentrations. The need for olivine to crystallize close to the liquidus suggests pressures around 200 MPa and limits liquidus temperatures to values around 1160°C.

Redox state

Oxidizing redox conditions have been commonly assumed at Stromboli (e.g. Metrich *et al.*, 2001; Salvioli-Mariani *et al.*, 2002). Previously, ΔNNO values $\geq 0{\cdot}5$ have been obtained from the proportions of S^{VI} species and Fe^{3+}/Fe^{2+} ratios measured *in situ* in melt inclusions (Metrich & Clocchiatti, 1996; Metrich *et al.*, 2002). ΔNNO >1·5 can be ruled out from our results, as this would lead to Fe–Ti oxide being a near-liquidus phase, which is not supported by the observed phenocryst assemblages or by the mineralogy of gabbroic cumulate nodules (Metrich *et al.*, 2001; Salvioli-Mariani *et al.*, 2002; Bertagnini *et al.*, 2003; Francalanci *et al.*, 2004). Application of the Mg-number (calculated with FeO) vs ΔNNO experimental correlation (Fig. 8) to diopsidic clinopyroxene phenocrysts and microphenocrysts from the golden pumice suggests redox conditions around ΔNNO = +0·5 for the magmas involved in the present-day activity, in agreement with the conclusions of Metrich *et al.* (2002)

VOLCANOLOGICAL IMPLICATIONS

The data presented in this study provide fundamental constraints on the physico-chemical conditions, volatile contents, redox state and crystallization processes in the magmas parental to the golden pumice. Therefore, applications in the context of the present-day activity of Stromboli volcano are numerous. Below, we restrict the discussion to three points: pre-

eruptive temperatures and H_2O contents, the structure of the deep feeding system and magma ascent paths.

Temperature and H_2O contents of present-day Stromboli magmas

A set of pre-eruptive parameters (i.e. temperature, melt H_2O content and redox state) has been precisely determined in this study for the golden pumice melt. These data allow the physical properties (e.g. viscosity, density, chemical diffusivities, etc.) of magmas sustaining explosions and paroxysms to be better estimated, a necessary step for the development of physical models to explain the present-day activity at Stromboli. For H_2O concentrations and redox state, the experimental constraints agree with measurements of melt inclusions. Average glass inclusion H_2O concentrations and experimentally derived melt H_2O contents overlap. Pre-eruptive temperatures are constrained from both melt inclusions and experiments. Temperature is known to better than ±50°C, probably to ±20°C (Fig. 11). The determined set of pre-eruptive P–T–H_2O parameters is internally consistent, as it is compatible with conditions on the liquidus surface.

There have been other attempts to determine magmatic conditions, mainly temperature, for Stromboli magmas. Salvioli-Mariani *et al*. (2002) obtained T_h values between 1134 and 1190°C for melt inclusions in clinopyroxene from gabbroic nodules from the Petrazza pyroclastics, an old (60–100 ka) Stromboli unit. T_h values between 1220 and 1250°C were found for melt inclusions in clinopyroxene phenocrysts from calc-alkaline magmas (see Vaggelli *et al*., 2003). For the present-day activity, various clinopyroxene–liquid and olivine–liquid geothermometers have been used by Francalanci *et al*. (2004), yielding values of either 1150–1325°C or 1190–1220°C for clinopyroxene and 1060–1150°C for olivine, both from the golden pumice. The significance of these thermometric data can be evaluated in the light of our experimental results. For example, clinopyroxene crystallization at 1190–1220°C on the liquidus would imply either, for a pressure of 200 MPa, a melt H_2O concentration <2·3 wt % or, for a melt H_2O concentration of 2·5–2·7 wt %, a pressure ≥300 MPa (Fig. 11). Although both sets of results are plausible, it is emphasized that temperatures of 1190–1220°C would imply a large (≥50°C; see Fig. 3) clinopyroxene + liquid crystallization interval. On the contrary, the crystal-poor nature of the golden pumices, and the presence of Fo-rich olivines (Fig. 9) and of compositionally primitive melt inclusions, constitute strong evidence for olivine crystallizing close to the liquidus or, in other words, for a small clinopyroxene + liquid crystallization/fractionation interval. Therefore, there are difficulties with clinopyroxene crystallization temperatures above 1150–1160°C. Clocchiatti (1981) obtained T_h of 1130°C for inclusions trapped in diopsidic zones of zoned clinopyroxene crystals, presumably from scoria. This value is in the range of T_h for inclusions in olivines from the golden pumices (1125–1140°C), and does not support clinopyroxene crystallization at temperatures much higher than those of olivine.

It is worth noting that temperatures and melt H_2O contents determined here strictly apply to the near-liquidus evolution of the golden pumice melts. Bertagnini *et al*. (2003) suggested temperatures around 1200°C (i.e. 40–60°C hotter than pre-eruptive temperatures inferred here) for the CaO-rich melts inferred to be parental to golden pumice.

Structure of the deep feeding system

Recent studies have suggested the presence of two physically separated magma reservoirs beneath Stromboli (e.g. Francalanci *et al*., 2004). The present-day activity taps a shallow reservoir, which is continuously erupted and replenished, where protracted clinopyroxene + olivine + plagioclase crystallization, coupled with magma mixing, occurs. This shallow-level

activity is sustained by the nearly continuous arrival of crystal-poor, volatile-rich melts (represented by the golden pumice), which come from a deep-seated reservoir (Francalanci *et al*., 2004). Overall, steady-state behavior is suggested between eruption, magma ascent and recharge, and presumably magma supply from the upper mantle; yet the marked differences in crystallinity, mineral chemistry (including compositional gaps) and melt inclusion volatile concentrations between scoria and pumices imply a discontinuous magmatic evolution, rather than a continuous one in the conduit–feeding system. These characteristics can be accounted for by the mush column model of Marsh (1996): the two magmatic stages recorded by scoria and pumices would represent local crystallization environments (each with specific physico-chemical conditions) in an essentially continuous feeding system.

The shallow magmatic stage recorded in scoria clearly corresponds to a preferential crystallization level, most probably associated with degassing and H_2O loss (Fig. 12b). The deep magmatic stage may be viewed as the level of storage of the golden pumice melts; that is, as the site where the golden pumice melts are processed from near-primary mantle melts, by crystallization, wall-rock–cumulate interaction and mixing (Di Carlo *et al*., in preparation). In this paper, conditions for the deep magmatic stage have been determined by constraining the near-liquidus evolution of the golden pumice melts (crystallization of primitive clinopyroxenes and olivines, entrapment of volatile-rich melt inclusions). A pressure range between 100 and 270 MPa, most probably around 200 MPa to allow olivine crystallization within 20°C to the liquidus, has been inferred. This converts to depths of 3·8–10·2 km (7·5 km for 200 MPa, taking a density of 2·7 g/cm^3 for the crustal layer below Stromboli; Barberi *et al*., 1994; Fig. 12a and b), within the metamorphic arc crust (e.g. Vaggelli *et al*., 2003; Salvioli-Mariani *et al*., 2005). The location of this deep magmatic level may be controlled by either a rheological discontinuity or a neutral buoyancy level between the magma and its wall-rocks (e.g. Corsaro & Pompilio, 2004). For comparison, hypocenters of the 1999 tectonic earthquake swarm at Stromboli have been located at a depth between 8 and 12 km (Falsaperla *et al*., 2003).

There are a few pressure determinations available for the Stromboli plumbing system that can be compared with the results of this study. Francalanci *et al*. (2004), although noting the relatively poor performance of clinopyroxene barometers at low pressures (some scoria samples failing to give meaningful results), found clinopyroxene equilibration pressures higher by 100–200 MPa in the pumice than in the scoria. Vaggelli *et al*. (2003), on the basis of fluid inclusion studies in quartzite nodules found in calc-alkaline magmas from ancient cycles of activity, determined two rest levels for Stromboli magmas, at 100 and 290 MPa. The 290 MPa pressure was obtained by taking a temperature of 1250°C along the isochore of the fluid system (Vaggelli *et al*., 2003). However, 1250°C may significantly overestimate magmatic temperatures, as discussed above. For a temperature of 1150°C, pressures around 250 MPa are obtained, near the upper bound of the range determined here (270 MPa). Although the feeding system geometries at Stromboli may have varied during the last 60–100 kyr, it is tempting to relate the deep rest level of Vaggelli *et al*. (2003) to the deep magmatic stage whose conditions have been determined in this study.

Metrich *et al*. (2001) and Bertagnini *et al*. (2003) found substantially higher pressures, from >400 MPa to slightly <300 MPa with a cluster near 350 MPa, based on the concentrations of dissolved H_2O and CO_2 in melt inclusions from golden pumice and the model of Papale (1999). In our view, these pressures represent maximum estimates for the deep magmatic stage, as our experimental results with H_2O–CO_2 mixtures indicate dissolved CO_2 concentrations in PST-9 glasses higher than predicted from existing solubility models (Di

Carlo *et al.*, in preparation). It should be noted that, for 350 MPa at 1140–1160°C on the liquidus, H_2O concentrations of 2·9–3·3 wt % (i.e. higher than the maximum frequency of H_2O concentrations in glass inclusions) are required (Fig. 11).

Magma ascent paths

The question arises of the fate of golden pumice melts once extracted from their storage level. Golden pumice magma ascent trajectories are shown in Fig. 12a. Initial conditions of the deep magmatic stage are set to 1150°C and 200 MPa for a melt H_2O content of about 2·6 wt % on the PST-9 liquidus surface (Figs 11 and 12a). Path (1) is an adiabat calculated with a slope of 5°C/100 MPa, appropriate for wet basaltic melts (6 wt % H_2O, Barclay & Carmichael, 2004). Although this slope maximizes ascent-related cooling of the golden pumice magma (H_2O melt 6 wt %), overall the degree of cooling along the adiabat is very small (Fig. 12a), as the pressure drop is at most 200 MPa. The path crosscuts in projection the constant aH_2O lines on the liquidus surface, aH_2O progressively increasing upon ascent. However, path (1) is steeper than the wt % H_2O contours. In other words, if closed-system conditions are assumed (neither loss nor gain of H_2O), the golden pumice melt should leave the liquidus surface and become superheated. It should be noted that this will persist until the wt % H_2O contours become steeper than path (1), which occurs from ~80 MPa along the ascent path (Fig. 12a). Therefore, if the golden pumice melt ascends along an adiabat, crystallization is not expected until shallow (<3 km) depths. For comparison, another ascent path defined by the initial and final (i.e. black scoria) *P*–*T* conditions [the latter taken from Bertagnini *et al.* (2003)], and arbitrarily assuming a linear *P*–*T* variation upon ascent, is shown in Fig. 12a [path (2)]. This only serves to illustrate continuous ascent-related crystallization, as H_2O contours are always steeper than path (2).

The crystal-poor nature of the golden pumices and the interpretation that their diopsidic clinopyroxene and Fo-rich olivine crystals are of deep provenance are both consistent with adiabatic magma ascent. However, the analysis above has ignored the possible presence of a fluid phase, which may be present at the storage level of the golden pumice melt and above. If this is the case, open-system conditions, rather than closed-system as in the analysis above, need to be considered for modelling magma ascent beneath Stromboli. In the presence of a fluid phase, a more elaborate treatment would be necessary and, therefore, the conclusions above should be viewed as preliminary.

CONCLUSIONS

In this paper, the evolution of a volatile-rich high-K basalt melt from the recent eruptive activity of Stromboli (PST-9) has been simulated experimentally at 1050–1175°C, 50–400 MPa, for melt H_2O concentrations between 1·2 and 5·5 wt % and ΔNNO ranging from –0·07 to +2·32. In most charges, quench crystallization was effectively suppressed by using a drop-quench technique. Fe loss was minimized, but not eliminated. Despite this problem, phase equilibrium results and compositions define a reliable dataset that sheds light on the evolution of the golden pumice melt.

Major crystallizing phases are clinopyroxene, olivine and plagioclase. Fe–Ti oxide is present in some charges. Clinopyroxene precedes olivine in the crystallization sequence and persists as the liquidus phase down to at least 200 MPa. This makes phase equilibria for PST-9 similar to those for ultra-calcic (ankaramitic) liquids from arc settings. Plagioclase is a late phase, in agreement with observed textural relations.

Clinopyroxene, olivine, plagioclase and glass composition vary systematically with the degree of crystallization. Diopsidic, Cr-rich and Al-, Ti-poor clinopyroxene phenocrysts in the golden pumice represent near-liquidus crystallization products. Ca in clinopyroxene sensitively depends on the H_2O content of the coexisting melt. The most Fo-rich olivines (Fo_{87}) are obtained at 100 and 200 MPa. With progressive crystallization, the glasses reach compositions within the shoshonite field.

A set of pre-eruptive liquidus *P*–*T*–melt H_2O concentration conditions (1140–1160°C, 100–270 MPa, 2·5–2·7 wt % H_2O in melt) is determined for the golden pumice melt by combining experimental and melt inclusion data. Near-liquidus clinopyroxene crystallization requires melt H_2O concentrations either <2·7–3·6 or 3 ± 1 wt %, overlapping with the maximum frequency of glass inclusion H_2O concentrations (2·5–2·7 wt % H_2O). The need to have olivine crystallizing close to the liquidus suggests pressures around 200 MPa and limits liquidus temperatures to values around 1160°C. Compositions of diopsidic clinopyroxene phenocrysts in the golden pumice suggest redox conditions around ΔNNO = +0·5. The set of pre-eruptive parameters determined here allows the physical properties of magmas sustaining explosions and paroxysms to be better evaluated.

Contrasts in crystallinity, mineral chemistry and melt inclusion volatile concentrations between scoria and pumices imply a discontinuous magmatic evolution in the conduit–feeding system. The deep magmatic stage, which is marked by the near-liquidus crystallization of primitive clinopyroxenes and olivines as well as by the entrapment of volatile-rich melt inclusions, corresponds to the storage region of the golden pumice melt. This occurs in the depth range 3·8–10·2 km (7·5 km for 200 MPa) within the metamorphic arc crust. For golden pumice melts adiabatically ascending from their storage region to the surface, no crystallization is expected. The shallow-level magmatic stage corresponds to a preferential crystallization level, most probably related to degassing and H_2O loss.

ACKNOWLEDGEMENTS

This paper forms part of the Ph.D. thesis of the first author. The experimental study on Stromboli was partially supported by an INGV–GNV Project (Eruptive Scenarios), by Galileo funds for Italy–France scientific co-operation and by funds for international co-operation from the University of Palermo. We wish to thank J. Barclay, A. Bertagnini and M. Carroll for their constructive reviews, and M. Wilson for her careful editorial work. Special thanks to Dr. M. Pompilio for the starting sample and his interest in this project.

REFERENCES

Albarède F. (1995) *Introduction to Geochemical Modelling* (Cambridge, Cambridge University Press) pp. 543.

Baker D. R. and Eggler D. H. (1987) Compositions of anhydrous and hydrous melts coexisting with plagioclase, augite and olivine or low-Ca pyroxene from 1 atm to 8 kbar: application to the Aleutian volcanic center of Atka. *American Mineralogist* **72:**12–28.

Barberi F., Rosi M., Sodi A. (1993) Volcanic hazard assessment at Stromboli based on review of historical data. *Acta Vulcanologica* **3:**173–187.

Barberi F., Gandino A., Gioncada A., La Torre P., Sbrana A., Zenucchini C. (1994) The deep structure of the Eolian arc (Filicudi–Panarea–Vulcano sector) in light of gravity, magnetic and volcanological data. *Journal of Volcanology and Geothermal Research* **61:**189–206.

Barclay J. and Carmichael I. S. E. (2004) A hornblende basalt from western Mexico: water-saturated phase relations constrain a pressure–temperature window of eruptibility. *Journal of Petrology* **45:**485–506.

Bartels K. S., Kinzler R. J., Grove T. L. (1991) High pressure phase relations of primitive high-alumina basalts from Medicine Lake volcano, northern California. *Contributions to Mineralogy and Petrology* **108:**253–270.

Behrens H., Romano C., Nowak M., Holtz F., Dingwell D. B. (1996) Near-infrared determination of water species in glasses of the system $MAlSi_3O_8$ (M = Li, Na, K): an interlaboratory study. *Chemical Geology* **128:**41–63.

Bertagnini A., Metrich N., Landi P., Rosi M. (2003) Stromboli volcano (Aeolian Archipelago, Italy): an open window on the deep-feeding system of a steady state basaltic volcano. *Journal of Geophysical Research* **108(B7):**2336 doi:10.1029/2002JB002146.

Burnham C. W. (1979) The importance of volatile constituents. In Yoder H. S. (Ed.). *The Evolution of Igneous Rocks* (Princeton University Press, Princeton, NJ) pp. 439–482.

Clocchiatti R. (1981) La transition augite–diopside et les liquides silicatés intra-cristallins dans les pyroclastes de l'activité actuelle du Stromboli: témoignages de la ré-injection et du mélange magmatiques. *Bulletin of Volcanology* **44:**339–357.

Conte A. M., Perinelli C., Trigila R. (2004) Cooling experiments on Stromboli lavas of different serial affinity giving variable crystal morphologies and phase compositions. Program and Abstracts of 2004 Workshop. *Reconstructing eruptive scenarios by field measurements, physical modelling and laboratory experiments* (INGV, Napoli) pp. 29–34.

Corsaro R. A. and Pompilio M. (2004) Buoyancy-controlled eruption of magmas at Mt Etna. *Terra Nova* **16:**16–22.

Costa F., Scaillet B., Pichavant M. (2004) Petrological and experimental constraints on the pre-eruption conditions of Holocene dacite from Volcán San Pedro (36°S, Chilean Andes)

and the importance of sulphur in silicic subduction-related magmas. *Journal of Petrology* **45:**855–881.

Danyushevsky L. V., Sokolov S., Falloon T. J. (2002) Melt inclusions in olivine phenocrysts: using diffusive re-equilibration to determine the cooling history of a crystal, with implications for the origin of olivine-phyric volcanic rocks. *Journal of Petrology* **43:**1651–1671.

Devine J. D., Gardner J. E., Brack H. P., Layne G. D., Rutherford M. J. (1995) Comparison of microanalytical methods for estimating H_2O contents of silicic volcanic glasses. *American Mineralogist* **80:**319–328.

Di Carlo I. (2004) Experimental simulation of pre-eruptive conditions of yellow pumice—Stromboli. Ph.D. thesis. , University of Palermo96.

Falloon T. J., Green D. H., Jacques A. L., Hawkins J. W. (1999) Refractory magmas in back-arc basin settings—experimental constraints on the petrogenesis of a Lau basin example. *Journal of Petrology* **40:**255–277.

Falsaperla S., Alparone S., Spampinato S. (2003) Seismic features of the June 1999 tectonic swarm in the Stromboli volcano region, Italy. *Journal of Volcanology and Geothermal Research* **125:**121–136.

Ferry J. M. and Baumgartner L. (1987) Thermodynamic models of molecular fluids at the elevated pressures and temperatures of the crustal metamorphism. In Eugster H. P. and Carmichael I. S. E. (Eds.). *Thermodynamic Modelling of Geological Materials: Minerals, Fluids and Melts. Mineralogical Society of America, Reviews in Mineralogy* **17:**323–365.

Francalanci L., Manetti P., Peccerillo A. (1989) Volcanological and magmatological evolution of Stromboli volcano (Aeolian Islands): the roles of fractional crystallization, magma mixing, crustal contamination and source heterogeneity. *Bulletin of Volcanology* **51:**355–378.

Francalanci L., Manetti P., Peccerillo A., Keller J. (1993) Magmatological evolution of the Stromboli volcano (Aeolian Arc, Italy): inferences from major and trace elements and Sr isotopic composition of lavas and pyroclastic rocks. *Acta Vulcanologica* **3:**127–151.

Francalanci L., Tommasini S., Conticelli S. (2004) The volcanic activity of Stromboli in the 1906–1998 AD period: mineralogical, geochemical and isotope data relevant to the understanding of the plumbing system. *Journal of Volcanology and Geothermal Research* **131:**179–211.

Gaetani G. A. and Grove T. L. (1998) The influence of water on the melting of mantle peridotite. *Contributions to Mineralogy and Petrology* **131:**323–346.

Gaetani G. A., Grove T. L., Bryan W. B. (1993) The influence of water on the petrogenesis of subduction-related igneous rocks. *Nature* **365:**332–334.

Ghiorso M. S. and Sack R. O. (1991) Fe–Ti oxide geothermometry: thermodynamic formulation and the estimation of the intensive variables in silicic magmas. *Contributions to Mineralogy and Petrology* **108:**485–510.

Gust D. A. and Perfit M. R. (1987) Phase relations of a high-Mg basalt from the Aleutian arc: implications for primary island arc basalts and high-Al basalts. *Contributions to Mineralogy and Petrology* **97:**7–18.

Holloway J. R. (1987) Igneous fluids. In Eugster H. P. and Carmichael I. S. E. (Eds.). *Thermodynamic Modelling of Geological Materials: Minerals, Fluids and Melts. Mineralogical Society of America, Reviews in Mineralogy* **17:**211–233.

Johnson M. C., Anderson A. T. Jr, Rutherford M. J. (1994) Pre-eruptive volatile contents of magmas. In Carroll M. R. and Holloway J. R. (Eds.). *Volatiles in Magmas. Mineralogical Society of America, Reviews in Mineralogy* **30:**281–330.

Kawamoto T. and Hirose K. (1994) Au–Pd sample containers for melting experiments on iron and water-bearing systems. *European Journal of Mineralogy* **6:**381–385.

Kress V. C. and Carmichael I. S. E. (1991) The compressibility of silicate liquids containing Fe_2O_3 and the effect of composition, temperature, oxygen fugacity and pressure on their redox states. *Contributions to Mineralogy and Petrology* **108:**82–92.

Landi P., Metrich N., Bertagnini A., Rosi M. (2004) Dynamics of magma mixing and degassing recorded in plagioclase at Stromboli (Aeolian Archipelago, Italy). *Contributions to Mineralogy and Petrology* **147:**213–227.

Lindsley D. H. and Frost B. R. (1992) Equilibria among Fe–Ti oxides, pyroxene, olivine and quartz: Part I. Theory. *American Mineralogist* **77:**987–1003.

Luhr J. F. and Carmichael I. S. E. (1980) The Colima volcanic complex, Mexico. I. Post-caldera andesites from volcán Colima. *Contributions to Mineralogy and Petrology* **71:**343–372.

Marsh B. (1996) Solidification fronts and magmatic evolution. *Mineralogical Magazine* **60:**5–40.

Martel C., Pichavant M., Bourdier J.-L., Traineau H., Holtz F., Scaillet B. (1998) Magma storage conditions and control of eruption regime in silicic volcanoes: experimental evidence from Mt. Pelée. *Earth and Planetary Science Letters* **156:**89–99.

Martel C., Pichavant M., Holtz F., Scaillet B., Bourdier J.-L., Traineau H. (1999) Effects of fO_2 and H_2O on andesite phase relations between 2 and 4 kbar. *Journal of Geophysical Research* **104:**29453–29470.

Médard E., Schmidt M. W., Schiano P. (2004) Liquidus surfaces of ultracalcic primitive melts: formation conditions and sources. *Contributions to Mineralogy and Petrology* **148:**201–215.

Metrich N. and Clocchiatti R. (1996) Sulfur abundance and its speciation in oxidized alkaline melts. *Geochimica et Cosmochimica Acta* **60:**4151–4160.

Metrich N., Bertagnini A., Landi P., Rosi M. (2001) Crystallization driven by decompression and water loss at Stromboli volcano (Aeolian Islands, Italy). *Journal of Petrology* **42:**1471–1490.

Metrich N., Bonnin-Mosbah M., Menez B., Galoisy L. (2002) Presence of sulfite (S^{IV}) in arc magmas: implications for volcanic sulfur emissions. *Geophysical Research Letters* **29(11):** doi:10.1029/2001GL14607.

Metrich N., Bertagnini A., Landi P., Rosi M., Belhadj O. (2005) Triggering mechanism at the origin of paroxysms at Stromboli (Aeolian Archipelago, Italy): the 5 April 2003 eruption. *Geophysical Research Letters* **32:**L10305 doi:10.1029/2004GL022257.

Morelli C., Giese P., Cassinis R., Colombi B., Guerra I., Luongo G., Scarascia S., Schutte K. G. (1975) Crustal structure of Southern Italy. A seismic refraction profile between Puglia, Calabria and Sicily. *Bollettino Geofisica Teorica ed Applicata* **17:**183–210.

Muncill G. E. and Lasaga A. C. (1987) Crystal-growth kinetics in igneous systems: one atmosphere experiments and application of a simplified growth model. *American Mineralogist* **72:**299–311.

O'Hara M. J. (1977) Geochemical evolution during fractional crystallization of a periodically refilled magma chamber. *Nature* **266:**503–507.

Papale P. (1997) Modeling of the solubility of a one-component H_2O or CO_2 fluid in silicate liquids. *Contributions to Mineralogy and Petrology* **126:**237–251.

Papale P. (1999) Modeling of the solubility of two-component H_2O–CO_2 fluid in silicate liquids. *American Mineralogist* **84:**477–492.

Pasquarè G., Francalanci L., Garduno V. H., Tibaldi A. (1993) Structure and geologic evolution of the Stromboli volcano, Aeolian Islands, Italy. *Acta Vulcanologica* **3:**79–89.

Peccerillo A. and Taylor S. R. (1976) Geochemistry of Eocene calc-alkaline rocks from Kastamonu area, northern Turkey. *Contributions to Mineralogy and Petrology* **58:**63–81.

Pichavant M., Martel C., Bourdier J.-J., Scaillet B. (2002a) Physical conditions, structure and dynamics of a zoned magma chamber: Mount Pelée (Martinique, Lesser Antilles arc). *Journal of Geophysical Research* **107(B5):** doi:10.1029/2001JB000315.

Pichavant M., Mysen B. O., Macdonald R. (2002b) Source and H_2O content of high-MgO magmas in island arc settings: an experimental study of a primitive calc-alkaline basalt from St. Vincent, Lesser Antilles arc. *Geochimica et Cosmochimica Acta* **66:**2193–2209.

Pownceby M. I. and O'Neill H.St.C. (1994) Thermodynamic data from redox reactions at high temperatures. III. Activity–composition relations in Ni–Pd alloys from EMF measurements at 850–1250 K and calibration of the NiO + Ni–Pd assemblage as a redox sensor. *Contributions to Mineralogy and Petrology* **116:**327–339.

Robie R. A., Hemingway B. S., Fisher J. R. (1979) Thermodynamic properties of minerals and related substances at 298·15 K and 1 bar (10^5 pascals) pressure and at higher temperatures. *US Geological Survey Bulletin* **1452:**456.

Roggensack K., Hervig R. L., McKnight S. B., Williams S. N. (1997) Explosive basaltic volcanism from Cerro Negro volcano: influence of volatiles on eruptive style. *Science* **277:**1639–1642.

Rosi M., Bertagnini A., Landi P. (2000) Onset of the persistent activity at Stromboli volcano (Italy). *Bulletin of Volcanology* **62:**294–300.

Roux J. and Lefevre A. (1992) A fast quench device for IHPV. *European Journal of Mineralogy* **4:**279–281.

Rutherford M. J., Sigurdsson H., Carey S. (1985) The May 18, 1980, eruption of Mount St. Helens, 1. Melt compositions and experimental phase equilibria. *Journal of Geophysical Research* **90:**2929–2947.

Salvioli-Mariani E., Mattioli M., Renzulli A., Serri G. (2002) Silicate melt inclusions in the cumulate minerals of gabbroic nodules from Stromboli volcano (Aeolian Islands, Italy): main components of the fluid phase and crystallization temperatures. *Mineralogical Magazine* **66:**969–984.

Salvioli-Mariani E., Renzulli A., Serri G., Holm P. M., Toscani L. (2005) Glass-bearing crustal xenoliths (buchites) erupted during the recent activity of Stromboli (Aeolian Islands). *Lithos* **81:**255–277.

Scaillet B. and Evans B. W. (1999) The 15 June 1991 eruption of Mount Pinatubo. I. Phase equilibria and pre-eruption P–T–$f$$O_2$–$f$$H_2O$ conditions of the dacite magma. *Journal of Petrology* **40:**381–411.

Scaillet B., Pichavant M., Roux J., Humbert G., Lefèvre A. (1992) Improvements of the Shaw membrane technique for measurements and control of $f$$H_2$ at high temperatures and pressures. *American Mineralogist* **77:**647–655.

Scaillet B., Pichavant M., Roux J. (1995) Experimental crystallization of leucogranite magmas. *Journal of Petrology* **36:**663–705.

Schiano P., Eiler J. M., Hutcheon I. D., Stolper E. M. (2000) Primitive CaO-rich, silica-undersaturated melts in island arcs: evidence for the involvement of clinopyroxene-rich lithologies in the petrogenesis of arc magmas. *Geochemistry, Geophysics, Geosystems* **1:**1999GC00032.

Sisson T. W. and Grove T. L. (1993a) Experimental investigation of the role of H_2O in calc-alkaline differentiation and subduction zone magmatism. *Contributions to Mineralogy and Petrology* **113:**143–166.

Sisson T. W. and Grove T. L. (1993b) Temperature and H_2O contents of low-MgO high alumina basalts. *Contributions to Mineralogy and Petrology* **113:**167–184.

Speranza F., Pompilio M., Sagnotti L. (2004) Paleomagnetism of spatter lavas from Stromboli volcano (Aeolian Islands, Italy): implications for the age of paroxysmal eruptions. *Geophysical Research Letters* **31:**L02607 doi:10.1029/20318944.

Taylor J. R., Wall V. J., Pownceby M. I. (1992) The calibration and application of accurate redox sensors. *American Mineralogist* **77:**284–295.

Vaggelli G., Francalanci L., Ruggieri G., Testi S. (2003) Persistent polybaric rests of calc-alkaline magmas at Stromboli volcano, Italy: pressure data from fluid inclusions in restitic quartzite nodules. *Bulletin of Volcanology* **65:**385–404.

Wallace P. J. (2005) Volatiles in subduction zone magmas: concentrations and fluxes based on melt inclusions and volcanic gas data. *Journal of Volcanology and Geothermal Research* **140:**217–240.

FIGURES

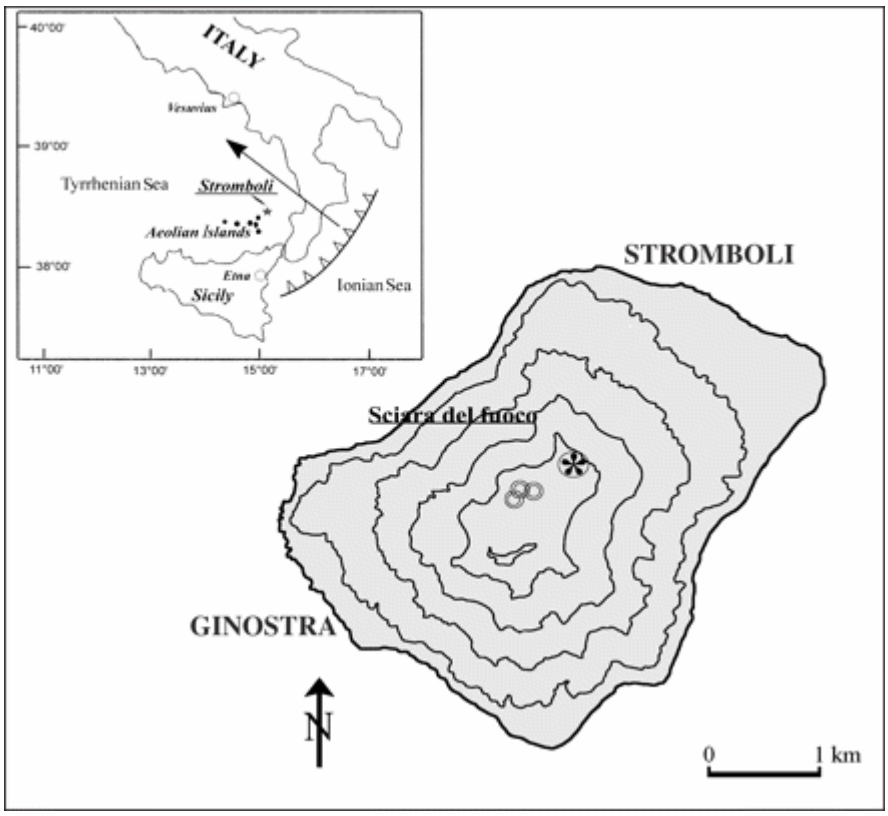

Fig. 1. Map of Stromboli island showing the summit craters (circles). The PST-9 starting material (star) comes from a trench dug near the summit of the volcano. The inset shows the location of Stromboli (star) within the Aeolian archipelago, and of Vesuvius and Etna volcanoes. The active subduction plane and direction are also indicated.

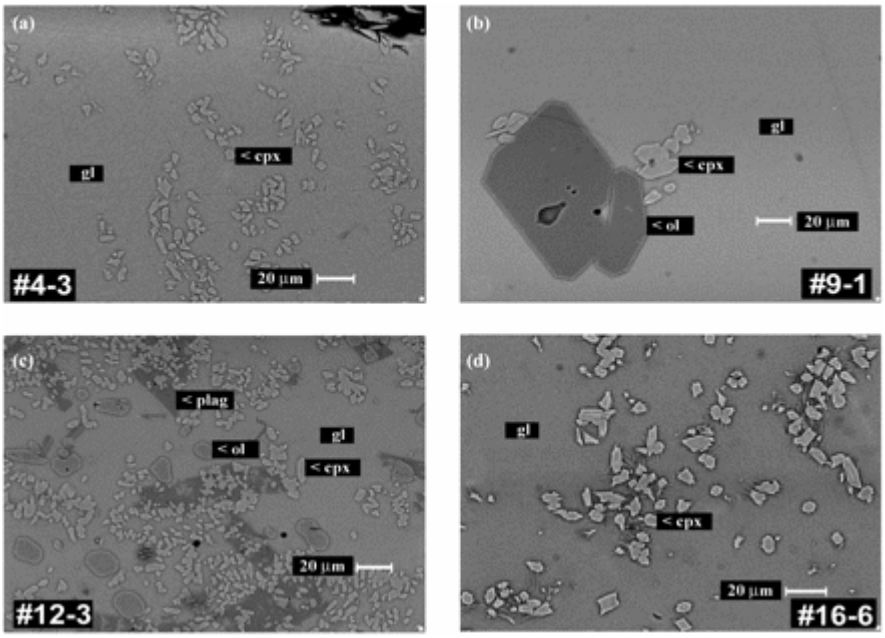

Fig. 2. Backscattered electron images of experimental charges. (See Tables 2 and 3 for experimental conditions.) (a) Typical clinopyroxene crystals in a high-temperature subliquidus charge (4-3). (b) Cotectic crystallization of clinopyroxene + olivine (charge 9-1). The difference in size between the two mineral phases should be noted. (c) Three-phase clinopyroxene + olivine + plagioclase assemblage (charge 12-3) with exceptionally large plagioclase crystals. (d) Illustration of quench crystallization textures with needles of phlogopite(?) nucleating on clinopyroxene (charge 16-6). In contrast, no such phases are present in (a), (b) or (c). gl, glass; cpx, clinopyroxene; ol, olivine; plag, plagioclase.

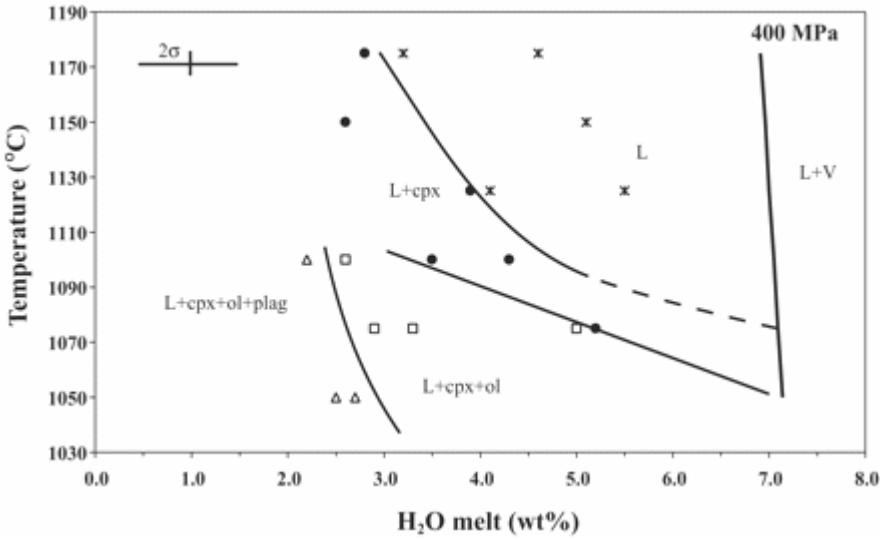

Fig. 3. Experimentally determined *T*–H_2O in melt phase diagram for PST-9 golden pumice at 400 MPa. Data are given in Table 2. The water saturation curve is calculated from Burnham (1979). L, liquid; V, vapor; cpx, clinopyroxene; ol, olivine; plag, plagioclase.

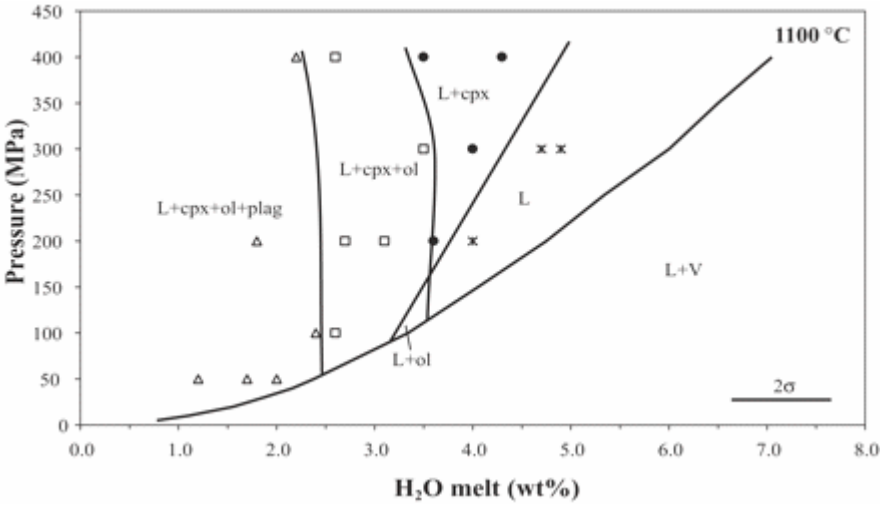

Fig. 4. Experimentally determined *P*–H_2O in melt phase diagram for PST-9 golden pumice at 1100°C. Data are given in Table 3. The water saturation curve is calculated from Burnham (1979). Abbreviations are as in Fig. 3.

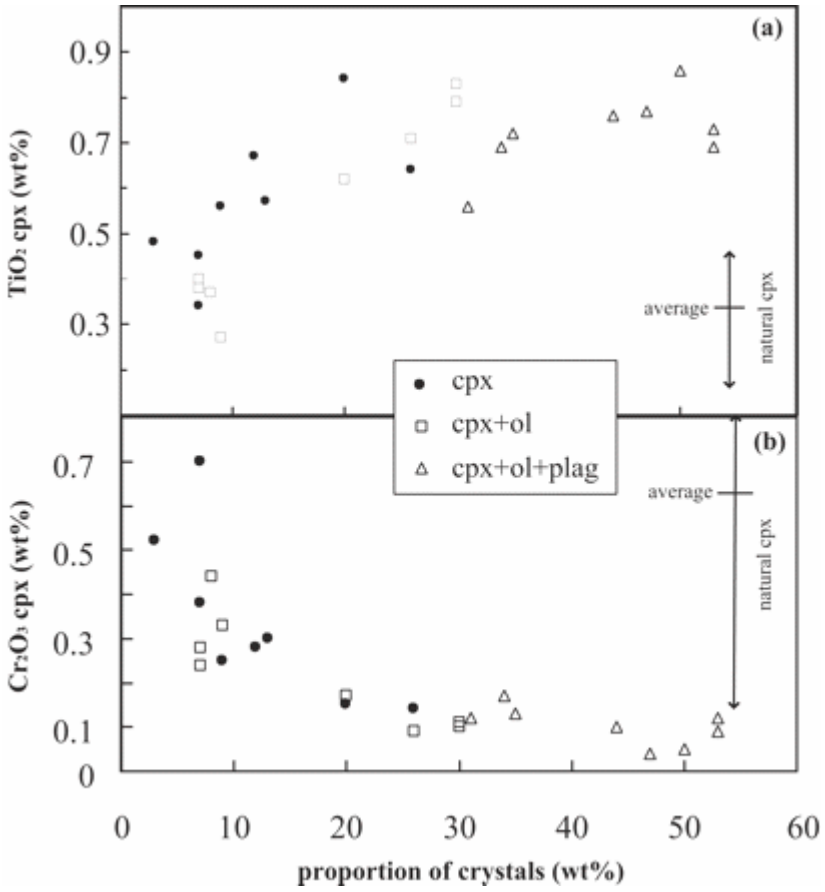

Fig. 5. Dependence of experimental clinopyroxene TiO_2 (a) and Cr_2O_3 (b) contents on the proportion of crystals in the charge (calculated by mass balance; see text). Data are subdivided by phase assemblage (cpx, cpx + ol, cpx + ol + plag). For comparison, the range (i.e. minimum, maximum) of TiO_2 (a) and Cr_2O_3 (b) contents in clinopyroxene phenocrysts and microphenocrysts from golden pumices is shown together with average values. It should be noted that only clinopyroxene compositions from the diopsidic group are compared (source of data: M. Pompilio, unpublished data; Di Carlo, 2004; Francalanci *et al*., 2004); that is, the range of clinopyroxene compositions typical of scoriae is not shown

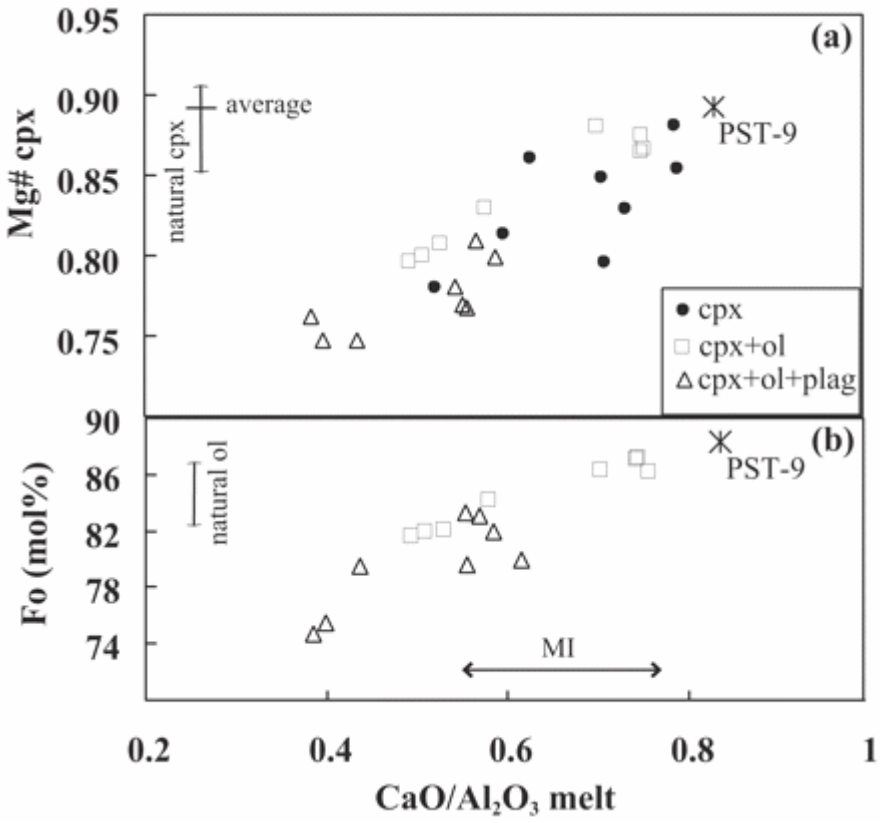

Fig. 6. Mg-number (calculated with FeO_t) in experimental clinopyroxenes (a) and Fo in experimental olivines (b) plotted as a function of the degree of differentiation (CaO/Al_2O_3) of coexisting melts. Data for PST-9 are from Table 1. The range of Mg-number in diopsidic clinopyroxene phenocrysts from golden pumice is shown for comparison (source of data as in Fig. 5), together with the average value. Compositions of homogeneous olivines considered to be in equilibrium with the golden pumices ($Fo_{83–87}$, Bertagnini *et al.*, 2003) and of their melt inclusions (MI) are also indicated.

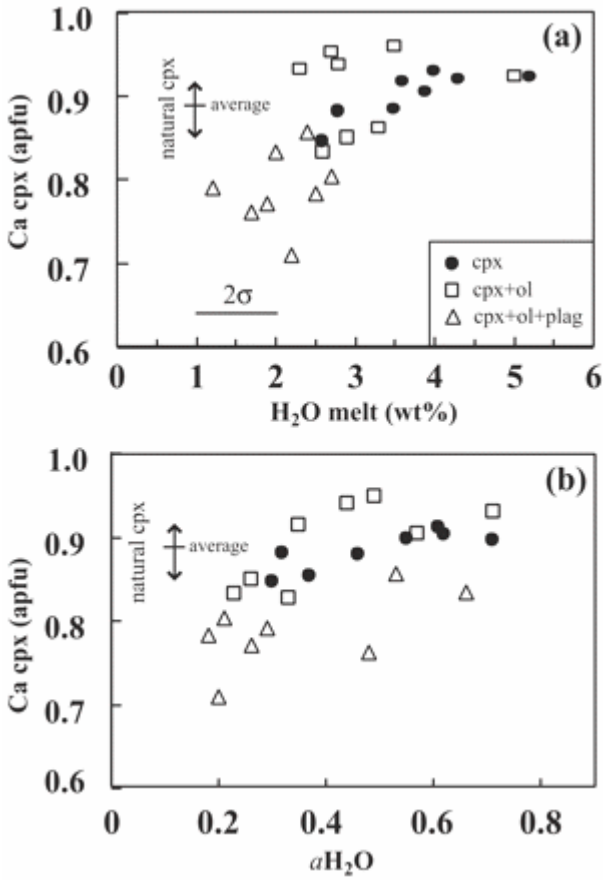

Fig. 7. Ca (a.p.f.u.) in experimental clinopyroxenes plotted as a function of (a) wt % H_2O in melt and (b) aH_2O, calculated from Burnham (1979) using melt compositions and experimental conditions from Tables 2–5. The influence of phase assemblage on the correlation should be noted. For comparison, the range of Ca in diopsidic clinopyroxene phenocrysts from the golden pumice is indicated (source of data as in Fig. 5), together with the average value.

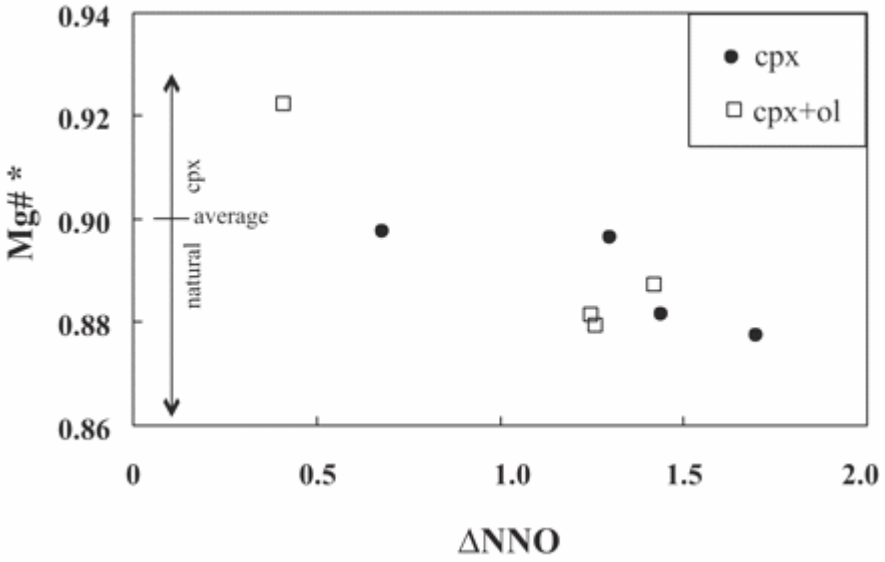

Fig. 8. Mg-number* (calculated with FeO) in experimental clinopyroxenes from near-liquidus charges plotted as a function of ΔNNO (see text). The entire range of Mg-number* in diopsidic clinopyroxene phenocrysts from the golden pumice is shown for comparison (source of data as in Fig. 5), together with the average value.

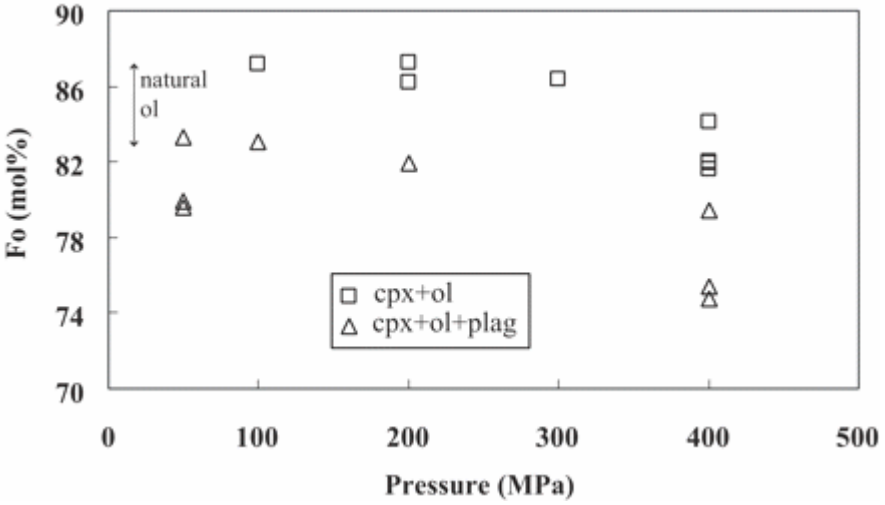

Fig. 9. Fo content of experimental olivines plotted as a function of pressure. The maximum in the range 100–200 MPa should be noted. Compositions of olivines considered to be in equilibrium with the golden pumices ($Fo_{83–87}$, Bertagnini *et al.*, 2003) are also shown.

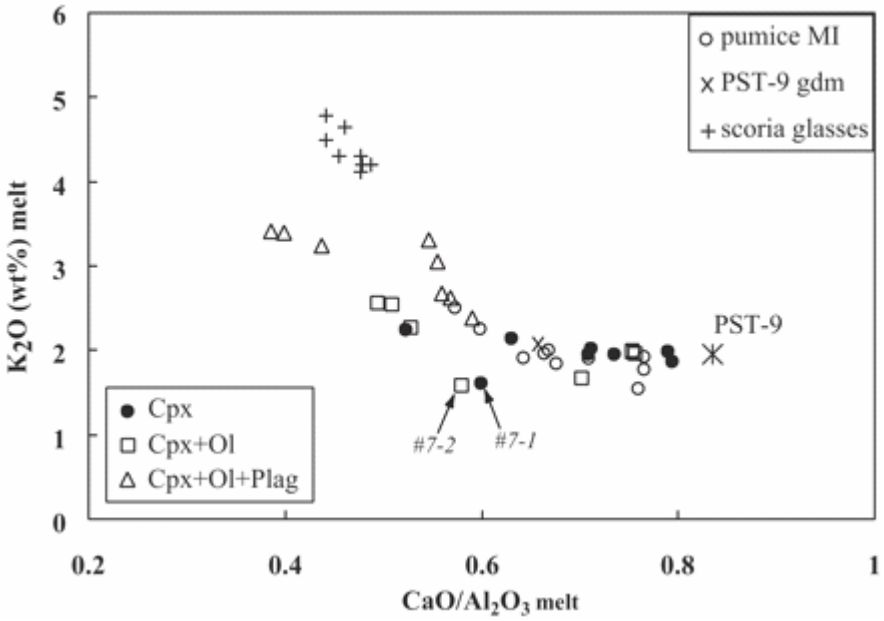

Fig. 10. Experimental melt compositions shown in a K_2O vs CaO/Al_2O_3 diagram, illustrating the increase of K_2O with progressive crystallization of the golden pumice melt. For comparison, compositions of the groundmass glass (gdm) in PST-9 (Table 1), of melt inclusions (MI) in $Fo_{83–87}$ olivines from pumices (Metrich *et al*., 2001; Bertagnini *et al*., 2003) and of interstitial glasses in scoriae (Francalanci *et al*., 2004; Landi *et al*., 2004) are shown. Glasses from charges 7-1 and 7-2 plot slightly below the main trend as a result of quench crystallization (see text).

TABLES

Table 1: Composition of PST-9 golden pumice and starting glass, and of phenocrysts, xenocrysts and groundmass

Label	PST-9[1]	Glass[2] (*n* = 9)[3]	Cpx mph/r	Cpx xe/r	Ol ph/r	Ol xe/c	Plag xe	Gdm (*n* = 10)
SiO_2	49·4	49·8(6)[4]	51·77	50·94	39·10	39·14	48·8	49·6 (5)
TiO_2	0·79	0·80(6)	0·27	0·70	0·00	0·00	0·00	0·84 (5)
Al_2O_3	15·75	15·0(3)	3·38	2·63	0·03	0·03	31·66	17·2 (2)
Fe_2O_3	1·3	n.d.	n.d.	n.d.	n.d.	n.d.	n.d.	n.d.
FeO	6·5	7·76(33)	3·54	9·48	11·92	21·89	0·85	7·10 (20)
MnO	0·15	0·10(9)	0·03	0·41	0·29	0·28	0·00	0·09 (5)
MgO	7·96	8·06(11)	16·56	14·52	47·61	38·90	0·08	6·41 (11)
CaO	12·73	12·1(3)	22·27	19·74	0·20	0·38	14·92	11·4 (2)
Na_2O	2·27	2·32(9)	0·26	0·33	0·00	0·00	2·36	2·58 (7)
K_2O	1·85	1·84(7)	0·00	0·00	0·00	0·00	0·38	2·07 (8)
P_2O_5	0·43	0·62(6)	n.d.	n.d.	n.d.	n.d.	n.d.	n.d.
Cr_2O_3	—	0·02(5)	0·83	0·09	0·01	0·00	0·05	0·03 (4)
NiO	—	0·02(3)	n.d.	n.d.	0·04	0·18	0·05	0·02 (4)
Total	99·1	98·5	98·91	98·84	99·20	100·80	99·07	97·3
			Wo 46	42	Fo 88	76	An 76	
			En 48	43	Fa 12	24	Ab 22	
			Fs 6	15			Or 2	

[1]Whole-rock analysis. The other values are electron microprobe data. Major elements (wt %) analysed by inductively coupled plasma atomic emission spectrometry (ICP-AES); total includes LOI = 0·62 wt %; trace elements analysed by ICP-mass spectrometry (ICP-MS) (Cr 259 ppm; Ni 75 ppm; Ba 920 ppm; La 45 ppm; Eu 2·0 ppm; Lu 0·3 ppm). Analysis performed at the Centre de Recherches Pétrographiques et Géochimiques (CRPG, Nancy, France).

[2]PST-9 glass.

[3]Number of electron microprobe analyses.

[4]One standard deviation in terms of least unit cited. Cpx, clinopyroxene; Ol, olivine; Plag, plagioclase; Gdm, groundmass; mph, microphenocryst; ph, phenocryst; xe, xenocryst; r, rim;

c, core. Cpx and Ol xenocrysts are identified from their composition (Metrich *et al*., 2001; Bertagnini *et al*., 2003). Plag is entirely xenocrystic (Landi *et al*., 2004). Xenocrysts are crystals from the crystal-rich resident black scoria (BS) magma incorporated and partially reacted in the golden pumice (GP) melt during eruption.

Table 2: Experimental results at 400 MPa

Charge	H_2O melt (wt %)	aH_2O[1]	log fO_2	ΔNNO	Phase[2] assemblage	ΣR^2	ΔFeO[3](%)	$K_{d\ Fe–Mg}^{cpx–liq}$	$K_{d\ Mg}^{ol–liq}$	$K_{d\ Ca–Na}^{plag–liq}$
Run 4, 1175°C, 416·8 MPa, 5 h, fH_2 *= 0·305 MPa,* X_{Ni} *= 0·18,* $Au_{70}Pd_{30}$[4]										
4-1	4·6[5]	0·65	–6·03	1·92	gl(100)	1·84	–8·40			
4-2	3·2[5]	0·42	–6·41	1·54	gl(100)	2·33	–12·10			
4-3	2·8	0·32	–6·64	1·30	gl(93) + cpx(7)	1·59	–15·20	0·36/0·41		
Run 3, 1150°C, 406·8 MPa, 14 h; fH_2 *= 0·199 MPa,* X_{Ni} *= 0·14,* $Au_{70}Pd_{30}$										
3-1	5·1[5]	0·72	–5·93	2·32	gl (100)	7·12	–24·10			
Run 14, 1150°C, 405·0 MPa, 19 h, fH_2 *= 0·465 MPa,* X_{Ni} *= 0·24,* $Au_{70}Pd_{30}$										
14-1[6]	2·5	0·25	–7·59	0·66	gl(n.d.) + cpx(n.d.)	n.d.	n.d.	0·43/0·33		
14-2[6]	2·0	0·18	–7·87	0·38	gl(n.d.) + cpx(n.d.)	n.d.	n.d.	0·53/0·41		
Run 21, 1150°C, 400·0 MPa, 21 h, fH_2 *= 0·594 MPa,* X_{Ni} *= 0·27,* $Ag_{70}Pd_{30}$										
21-4	2·6	0·30	–7·65	0·60	gl(88) + cpx(12)	2·37	–17·70	0·45/0·46		
Run 5, 1125°C, 402·8 MPa, 15 h, fH_2 *= 0·677 MPa,* X_{Ni} *= 0·30,* $Au_{70}Pd_{30}$										
5-1	5·5	0·77	–7·29	1·26	gl(100)	4·85	–21·60			
5-2	4·1	0·55	–7·58	0·86	gl(100)	6·33	–23·50			
5-3	3·9	0·46	–7·74	0·81	gl(87) + cpx(13)	5·91	–29·40	0·35/0·34		

Run 6, 1100°C, 404·3 MPa, 17 h, fH_2 *= 0·903 MPa,* X_{Ni} *= 0·36,* $Au_{70}Pd_{30}$										
6-1	4·3	0·55	–8·19	0·68	gl(91) + cpx(9)	4·01	–23·80	0·29/0·34		
6-4	2·6	0·23	–8·94	–0·07	gl(70) + cpx(27) + ol(3)	4·02	–23·10	0·40/0·39	0·42/0·34	
Run 10, 1100°C, 399·4 MPa, 21 h, fH_2 *= 0·109 MPa,* X_{Ni} *= 0·10,* $Au_{90}Pd_{10}$										
10-1	3·5	0·37	–6·86	2·01	gl(74) + cpx(26) + ox(tr)	0·63	–7·30	0·39/0·36		
10-2	2·2	0·20	–7·24	1·63	gl(47) + cpx(40) + ol(3) + plg(11) + ox(tr)	0·90	–9·60	0·48/0·32	0·37/0·25	1·68
Run 7, 1075°C, 408·2 MPa, 16·5 h, fH_2 *= 0·557 MPa,* X_{Ni} *= 0·29,* $Au_{70}Pd_{30}$										
7-1	5·2	0·62	–8·03	1·17	gl(80) + cpx(20) + qu	3·18	–18·30	0·44/0·33		
7-2	5·0	0·57	–8·10	1·10	gl(80) + cpx(17) + ol(3) + qu	2·27	–15·60	0·22/0·28	0·36/0·26	
7-3	3·3	0·33	–8·57	0·62	gl(74) + cpx(24) + ol(2) + qu	2·41	–17·60	0·41/0·24	0·46/0·31	
7-4	2·9	0·26	–8·78	0·41	gl(70) + cpx(27) + ol(3)	2·97	–19·70	0·36/0·37	0·42/0·33	
Run 11, 1050°C; 393·1 MPa, 16 h, fH_2 *= 0·469 MPa,* X_{Ni} *= 0·27,* $Au_{90}Pd_{10}$										
11-7	2·7	0·21	–9·24	0·30	gl(50) + cpx(35) + ol(4) + plg (11)	0·19	–3·70	0·30/0·27	0·34/0·26	2·42
11-4	2·5	0·18	–9·37	0·16	gl(47) + cpx(36) + ol(4) + plg(13)	1·09	–10·2	0·29/0·25	0·34/0·27	2·15

[1] $a$$H_2O$ calculated from H_2O melt using the model of Burnham (1979) and melt compositions from Table 4; X_{Ni} is mole fraction of Ni in the alloy phase of the sensor; log fO_2 calculated from experimental fH_2 and fH_2O (determined from aH_2O); ΔNNO = log fO_2 – log fO_2 of the

NNO buffer calculated at *P* and *T* (Pownceby & O'Neill, 1994); n.d., not determined; tr: a trace of (phase proportion <1% by weight).

[2]Phase proportions calculated by mass balance; gl, glass; cpx, clinopyroxene; ol, olivine; plag, plagioclase; ox, Fe–Ti oxide; qu, quench crystals detected by SEM.

[3]Apparent loss or gain of FeO (Fe = FeO_t) calculated as 100 x (FeO_{calc} – $FeO_{starting\ sample}$)/$FeO_{starting\ sample}$. FeO_{calc} and ΣR^2 are obtained from the mass-balance calculations.

[4]Capsule material.

[5]H_2O analyzed by Karl-Fischer titration. For the other charges, H_2O analyzed with the by-difference method.

[6]Starting material is PST-9 + 10 wt % FeO. Mass-balance calculations were not performed.

$K_{d\ cpx–liq}^{Fe–Mg}$= (Fe/Mg in cpx)/(Fe/Mg in melt), $K_{d\ ol–liq}^{Fe–Mg}$= (Fe/Mg in ol)/(Fe/Mg in melt), $K_{d\ plag–liq}^{Ca–Na}$= (Ca/Na in plag)/(Ca/Na in melt). For cpx–liq and ol–liq, the first K_d is calculated with FeO = FeO and the second with FeO = FeO_t (see text).

Table 3: Experimental results at 1100°C

Charge	H_2O melt (wt %)	aH_2O	log fO_2	Δ NNO	Phase assemblage	ΣR^2	Δ FeO (%)	$K_{d\ cpx–liq}^{Fe–Mg}$	$K_{d\ ol–liq}^{Fe–Mg}$	$K_{d\ plag–liq}^{Ca–Na}$
Run 16, 1100°C, 308·0 MPa, 17 h, fH_2 *= 0·305 MPa,* X_{Ni} *= 0·24,* $Au_{90}Pd_{10}$										
16-6	3·5	0·49	–7·63	1·25	gl(91) + cpx(8) + ol(1) + qu	0·69	–5·50	0·29/0·20	0·34/0·23	
16-7	4·0	0·61	–7·44	1·44	gl(97) + cpx(3) + qu	0·43	–7·00	0·35/0·23		
Run 20, 1100°C, 300·0 MPa, 17 h, fH_2 *= 0·289 MPa,* X_{Ni} *= 0·23,* $Au_{90}Pd_{10}$										
20-1	4·9	0·83	–7·13	1·75	gl(100)	1·55	–8·30			
20-2	4·7	0·78	–7·18	1·70	gl(100)	1·66	–8·50			
Run 15, 1100°C; 209·0 MPa, 21 h, fH_2 *= 0·181 MPa,* X_{Ni} *= 0·22,* $Au_{90}Pd_{10}$										
15-1	3·1	0·53	–7·48	1·42	gl(93) + cpx(5) + ol(2) + qu	0·27	–6·00	0·29/0·25	0·33/0·23	

15-3	2·7	0·44	–7·64	1·26	gl(93) + cpx(5) + ol(2) + qu	0·23	–5·20	0·32/0·24	0·37/0·25	
Run 19, 1100°C, 200·0 MPa, 15 h, fH_2 *= 0·177 MPa,* X_{Ni} *= 0·22,* $Au_{90}Pd_{10}$										
19-2	4·0	0·84	–7·05	1·85	gl(100)	1·31	–7·60			
19-3[1]	1·8	0·23	–8·17	0·72	gl(65) + cpx(28) + ol(3) + plg(4)	0·14	–3·60	0·45/0·32	0·33/0·24	
19-4	3·6	0·71	–7·20	1·70	gl(97) + cpx(3) + qu	1·04	–10·50	0·39/0·30		
Run 9, 1100°C, 102·9 MPa, 17 h, fH_2 *= 0·347 MPa,* X_{Ni} *= 0·47,* $Au_{90}Pd_{10}$										
9-1	2·6	0·64	–8·51	0·41	gl(93) + cpx(4) + ol(3)	0·43	–7·40	0·18/0·22	0·31/0·23	
Run 18, 1100°C, 100·0 MPa, 25·5 h, fH_2 *= 0·120 MPa,* X_{Ni} *= 0·26,* $Au_{90}Pd_{10}$										
18-1	2·4	0·53	–7·72	1·19	gl(66) + cpx(20) + ol(5) + plg(9)	1·19	–11·50	0·28/0·26	0·33/0·23	2·53
Run 12, 1100°C, 48·4 MPa, 20 h, fH_2 *= 0·095 MPa,* X_{Ni} *= 0·34,* $Au_{90}Pd_{10}$										
12-3	2·0	0·66	–7·99	0·93	gl(69) + cpx(19) + ol(5) + plg(7)	1·95	–14·20	0·35/0·29	0·33/0·23	2·06
12-2	1·2	0·29	–8·71	0·22	gl(53) + cpx(24) + ol(7) + plg(16)	1·89	–14·01	0·37/0·27	0·32/0·24	2·23
12-1	1·7	0·48	–8·27	0·66	gl(56) + cpx(27) + ol(6) +plg(11)	0·80	–8·90	0·38/0·28	0·32/0·24	1·56

Notation and abbreviations are as in Table 2.

[1]$Ag_{70}Pd_{30}$ capsule.

Table 4: Experimental compositions at 400 MPa

Charge	Phase	SiO_2	TiO_2	Al_2O_3	FeO	MnO	MgO	CaO	Na_2O	K_2O	Cr_2O_3	NiO	P_2O_5	Total	Mol %
PST-9	gl[1](9)[2]	50·6(6)[3]	0·81(6)	15·2(3)	7·88(33)	0·10(9)	8·19(11)	12·3(3)	2·36(9)	1·87(7)	0·02(5)	0·02(3)	0·63(6)	98·5	
4-1	gl(8)	51·3(3)	0·86(8)	15·1(1)	7·58(24)	0·19(8)	7·73(7)	12·6(1)	2·21(7)	1·77(6)	0·07(7)	0·03(6)	0·63(5)	92·4	
4-2	gl(9)	51·3(4)	0·87(5)	15·1(2)	7·28(33)	0·09(9)	7·79(13)	12·6(3)	2·32(9)	1·87(10)	0·04(5)	0·05(6)	0·66(5)	94·0	
4-3	gl(5)	49·8(5)	0·73(7)	16·8(4)	7·16(36)	0·10(7)	7·99(12)	12·4(4)	2·40(3)	1·93(8)	0·05(6)	0·04(6)	0·60(8)	93·5	
	cpx(7)	48·9(12)	0·45(15)	5·38(66)	5·60(61)	0·12(9)	15·3(5)	21·9(4)	0·34(5)	0·09(4)	0·38(7)	0·05(6)	n.d.	98·5	$En_{47}Wo_{48}$
3-1	gl(9)	52·0(6)	0·87(7)	15·2(2)	6·28(19)	0·16(9)	7·91(12)	12·7(2)	2·30(10)	1·87(6)	0·04(6)	0·02(4)	0·68(7)	91·4	
14-1	gl(11)	52·1(2)	0·91(6)	17·5(2)	6·42(26)	0·16(11)	6·64(10)	11·2(3)	2·65(7)	2·31(9)	0·03(5)	0·07(6)	n.d.	93·4	
	cpx(5)	51·3(8)	0·36(19)	3·63(60)	5·13(115)	0·13(7)	15·9(8)	21·1(3)	0·26(4)	0·05(2)	0·14(9)	0·03(3)	n.d.	98·04	$En_{47}Wo_{45}$
14-2	gl(11)	52·8(3)	0·92(6)	18·1(2)	5·17(27)	0·16(5)	6·58(17)	11·2(2)	2·78(9)	2·29(13)	0·04(6)	0·01(4)	n.d.	93·95	
	cpx(4)	52·1(10)	0·63(12)	6·33(126)	4·62(64)	0·07(8)	14·3(9)	19·8(10)	0·52(26)	0·33(27)	0·17(4)	0·07(11)	n.d.	98·9	$En_{46}Wo_{46}$
21-4	gl(10)	51·9(3)	0·93(7)	16·2(2)	7·02(24)	0·13(8)	7·07(19)	11·5(3)	2·56(16)	2·00(6)	0·02(3)	0·02(3)	0·71(7)	95·1	
	cpx(13)	48·6(6)	0·67(12)	7·11(79)	6·43(75)	0·12(9)	14·0(5)	21·3(6)	0·47(9)	0·16(9)	0·28(11)	0·04(7)	0·35(9)	99·5	$En_{44}Wo_{48}$
5-1	gl(7)	50·9(7)	0·82(6)	16·2(2)	6·20(10)	0·07(5)	8·40(18)	12·6(2)	2·23(7)	1·90(9)	0·04(6)	0·01(3)	0·65(10)	90·6	
5-2	gl(6)	51·0(5)	0·81(9)	16·0(2)	6·36(20)	0·07(5)	8·28(17)	12·6(1)	2·34(6)	1·85(5)	0·10(8)	0·02(4)	0·63(5)	90·9	
5-3	gl(8)	51·2(7)	0·86(9)	17·9(2)	6·03(29)	0·12(10)	7·13(31)	11·3(3)	2·56(16)	2·13(14)	0·03(6)	0·01(2)	0·77(9)	92·4	
	cpx(7)	50·2(10)	0·57(15)	5·02(102)	4·50(74)	0·11(8)	15·6(7)	22·1(4)	0·28(6)	0·11(6)	0·30(18)	0·02(4)	n.d.	98·84	$En_{47}Wo_{48}$
6-1	gl(9)	52·1(2)	0·85(6)	16·4(2)	6·63(27)	0·25(12)	7·08(17)	11·6(3)	2·46(12)	1·93(4)	0·04(6)	0·03(4)	0·66(10)	93·0	
	cpx(9)	50·6(18)	0·56(24)	4·60(158)	5·03(97)	0·13(9)	15·8(9)	22·8(7)	0·27(7)	0·06(7)	0·25(13)	0·09(10)	n.d.	100·07	$En_{46}Wo_{48}$
6-4	gl(8)	52·7(4)	0·95(8)	18·9(3)	6·06(22)	0·18(6)	5·24(15)	9·62(22)	2·94(10)	2·53(9)	0·02(3)	0·03(3)	0·83(8)	95·2	

	cpx(6)	49·5(6)	0·79(8)	7·57(99)	6·52(50)	0·24(13)	14·4(4)	20·9(6)	0·54(22)	0·20(17)	0·11(8)	0·02(3)	n.d.	100·75	$En_{44}Wo_{46}$
	ol(5)	40·0(2)	0·03(3)	0·04(3)	17·4(6)	0·36(22)	44·10(3)	0·29(2)	0·03(3)	0·03(5)	0·04(5)	0·07(6)	n.d.	102·4	Fo_{82}
10-1	gl(10)	51·9(3)	0·87(11)	18·1(2)	8·05(34)	0·20(11)	5·70(22)	9·45(34)	2·73(16)	2·23(10)	0·03(4)	0·03(4)	0·78(7)	94·0	
	cpx(16)	48·0(7)	0·64(12)	6·53(70)	6·94(55)	0·13(10)	13·8(5)	21·5(6)	0·37(9)	0·10(11)	0·14(9)	0·05(7)	0·25(5)	98·5	$En_{43}Wo_{48}$
10-2	gl(11)	52·9(5)	1·06(8)	18·0(4)	8·12(35)	0·16(9)	4·34(49)	7·87(69)	3·26(15)	3·25(15)	0·01(1)	0·00(0)	1·03(10)	95·7	
	cpx(4)	48·8(5)	0·73(5)	8·05(81)	7·83(23)	0·19(7)	13·0(7)	17·8(9)	0·83(22)	0·51(29)	0·09(6)	0·00(0)	n.d.	97·8	$En_{43}Wo_{42}$
	ol(3)	38·5(2)	0·02(3)	0·12(11)	18·5(5)	0·28(5)	40·1(6)	0·26(11)	0·00(0)	0·02(2)	0·00(0)	0·00(0	n.d.	97·8	Fo_{79}
	plag(3)	50·3(3)	0·13(8)	29·1(104)	1·26(21)	0·00(0)	0·37(22)	13·3(9)	3·27(19)	0·79(26)	0·04(7)	0·06(10)	n.d.	98·5	$An_{66}Or_{5}$
7-1	gl(8)	53·1(3)	0·92(7)	17·8(6)	7·26(33)	0·14(8)	5·91(30)	10·7(9)	2·50(14)	1·59(61)	0·02(3)	0·03(4)	n.d.	90·3	
	cpx(7)	48·9(16)	0·84(31)	6·02(156)	5·99(156)	0·16(6)	14·6(8)	22·7(7)	0·28(6)	0·06(3)	0·15(11)	0·02(4)	n.d.	99·7	$En_{44}Wo_{49}$
7-2	gl(7)	52·8(7)	0·89(7)	18·4(4)	7·26(35)	0·16(7)	5·64(64)	10·7(3)	2·61(7)	1·58(23)	n.d.	n.d.	n.d.	90·3	
	cpx(5)	49·6(14)	0·62(10)	5·28(117)	5·52(111)	0·13(10)	15·2(9)	22·7(9)	0·33(12)	0·11(16)	0·17(3)	0·02(4)	n.d.	99·7	$En_{46}Wo_{49}$
	ol(6)	40·2(5)	0·01(2)	0·01(2)	15·3(8)	0·26(12)	45·4(5)	0·22(5)	0·01(2)	0·01(2)	0·05(6)	0·07(8)	n.d.	101·6	Fo_{84}
7-3	gl(8)	52·5(3)	0·94(7)	18·9(2)	6·90(54)	0·17(12)	5·56(24)	9·99(29)	2·80(16)	2·26(9)	n.d.	n.d.	n.d.	92·8	
	cpx(5)	49·9(9)	0·71(14)	6·39(148)	6·37(63)	0·13(15)	14·9(7)	21·1(13)	0·43(25)	0·18(21)	0·09(6)	0·02(4)	n.d.	100·24	$En_{45}Wo_{46}$
	ol(7)	39·9(4)	0·01(1)	0·02(2)	17·2(9)	0·19(14)	44·2(4)	0·23(5)	0·02(3)	0·01(1)	0·02(3)	0·07(9)	n.d.	101·8	Fo_{82}
7-4	gl(8)	52·7(4)	0·97(5)	19·4(3)	6·48(36)	0·17(10)	5·25(15)	9·56(27)	2·95(13)	2·55(9)	n.d.	n.d.	n.d.	93·24	
	cpx(6)	48·8(7)	0·83(11)	7·33(108)	6·44(69)	0·19(10)	14·2(7)	21·4(9)	0·47(20)	0·24(20)	0·10(7)	0·04(5)	n.d.	99·9	$En_{44}Wo_{48}$
	ol(3)	40·1(2)	0·01(2)	0·06(3)	17·6(6)	0·19(19)	43·8(1)	0·23(4)	0·01(1)	0·01(2)	0·03(4)	0·09(11)	n.d.	102·1	Fo_{82}
11-7	gl(8)	53·5(4)	1·01(7)	18·8(1)	8·33(26)	0·16(10)	3·78(15)	7·52(18)	3·46(12)	3·39(10)	n.d.	n.d.	n.d.	93·5	
	cpx(5)	48·9(7)	0·86(10)	7·19(93)	8·21(55)	0·18(8)	13·7(4)	20·2(6)	0·50(7)	0·19(9)	0·05(8)	0·02(2)	n.d.	100·0	$En_{43}Wo_{45}$
	ol(3)	38·9(3)	0·00(0)	0·06(6)	22·2(2)	0·26(9)	38·3(1)	0·23(7)	0·03(1)	0·01(1)	0·00(0)	0·03(5)	n.d.	100·0	Fo_{75}
	plag(3)	49·3(2)	0·11(6)	29·3(9)	1·62(28)	0·17(29)	0·65(22)	14·3(6)	2·73(21)	0·78(6)	0·00(0)	0·07(12)	n.d.	99·1	$An_{71}Or_{5}$

11-4	gl(6)	54·1(9)	1·04(8)	19·5(106)	7·45(65)	0·17(3)	3·34(34)	7·50(81)	3·50(10)	3·41(25)	n.d.	n.d.	n.d.	94·8	
	cpx(4)	50·1(8)	0·69(7)	6·24(30)	8·11(16)	0·20(14)	14·6(5)	19·7(100)	0·46(13)	0·17(14)	0·12(9)	0·01(2)	n.d.	100·3	$En_{44}Wo_{43}$
	ol(3)	38·8(3)	0·00(0)	0·03(3)	22·9(3)	0·34(3)	38·1(3)	0·22(12)	0·01(1)	0·01(1)	0·00(0)	0·12(10)	n.d.	100·5	Fo_{75}
	plag(2)	49·7(7)	0·06(1)	29·4(5)	1·54(37)	0·12(15)	0·59(10)	13·7(1)	2·97(36)	0·82(2)	0·00(0)	0·01(1)	n.d.	98·8	$An_{68}Or_5$

[1]Glass analyses normalized to 100% anhydrous, with all Fe as FeO. Unnormalized total is reported.

[2]Number of microprobe analyses.

[3]One standard deviation in terms of least unit cited.

gl, glass; cpx, clinopyroxene; ol, olivine; plag, plagioclase; n.d., not determined. En = 100 x at. Mg/(Mg + Fe + Ca); Wo = 100 x at. Ca/(Mg + Fe + Ca) in pyroxene, calculated with Fe = FeO; Fo = 100 x at. Mg/(Mg + Fe) in olivine, calculated with Fe = FeO_t; An = 100 x at. Ca/(Ca + Na + K); Or = 100 x at. K/(Ca + Na + K) in plagioclase. PST-9 glass is from Table 1.

Table 5: Experimental compositions at 1100°C

Charge	Phase	SiO_2	TiO_2	Al_2O_3	FeO	MnO	MgO	CaO	Na_2O	K_2O	Cr_2O_3	NiO	P_2O_5	Total	Mol %
PST-9	gl[1](9)[2]	50·6(6)[3]	0·81(6)	15·2(3)	7·88(33)	0·10(9)	8·19(11)	12·3(3)	2·36(9)	1·87(7)	0·02(5)	0·02(3)	0·63(6)	98·5	
16-6	gl(8)	51·6(2)	0·88(5)	16·5(2)	8·27(29)	0·19(8)	6·80(18)	11·6(2)	2·51(14)	1·66(27)	0·02(3)	0·03(3)	n.d.	92·5	
	cpx(3)	53·7(7)	0·27(4)	2·54(50)	3·94(32)	0·04(7)	16·3(3)	23·8(4)	0·17(6)	0·11(3)	0·33(7)	0·10(10)	n.d.	101·3	$En_{46}Wo_{48}$
	ol(1)	41·31	0·00	0·01	12·7	0·13	45·12	0·23	0·00	0·00	0·00	0·01	n.d.	99·5	Fo_{86}
16-7	gl(8)	51·0(9)	0·88(5)	15·6(3)	7·94(28)	0·17(5)	7·67(15)	12·3(3)	2·36(5)	1·96(9)	0·02(4)	0·05(6)	n.d.	91·9	
	cpx(2)	53·5(10)	0·34(14)	2·75(108)	3·87(36)	0·10(14)	16·1(3)	23·6(1)	0·25(3)	0·01(2)	0·70(13)	0·10(14)	n.d.	101·4	$En_{46}Wo_{48}$
20-1	gl(11)	50·7(7)	0·81(6)	16·0(2)	7·44(34)	0·20(11)	7·91(21)	12·4(2)	2·13(9)	1·73(14)	0·04(6)	0·04(6)	0·67(12)	91·6	
20-2	gl(11)	50·5(6)	0·78(6)	16·0(3)	7·58(21)	0·17(8)	7·99(16)	12·3(2)	2·19(9)	1·75(8)	0·05(6)	0·03(4)	0·71(9)	91·7	
15-1	gl(8)	50·6(2)	0·91(9)	16·1(28)	7·91(28)	0·21(7)	6·99(28)	12·1(3)	2·49(15)	1·98(8)	0·04(4)	0·03(5)	0·67(6)	92·8	
	cpx(2)	52·5(3)	0·40(2)	2·76(14)	4·58(22)	0·21(18)	16·5(6)	23·0(5)	0·20(0)	0·00(0)	0·24(4)	0·04(6)	n.d.	100·4	$En_{47}Wo_{47}$
	ol(5)	40·5(3)	0·05(3)	0·05(1)	12·3 (8)	0·18(9)	47·2(7)	0·29(4)	0·03(1)	0·00(0)	0·02(3)	0·06(4)	n.d.	100·6	Fo_{87}
15-3	gl(8)	50·9(2)	0·88(8)	16·2(2)	8·00(41)	0·19(5)	7·00(15)	12·3(2)	2·45(12)	1·95(8)	0·05(6)	0·08(8)	n.d.	93·6	
	cpx(3)	53·2(2)	0·38(5)	2·98(24)	4·45(25)	0·03(4)	16·3(3)	23·6(2)	0·21(6)	0·07(1)	0·28(13)	0·04(6)	n.d.	101·5	$En_{46}Wo_{48}$
	ol(6)	40·5(6)	0·01(2)	0·02(2)	13·3(4)	0·28(7)	46·7(5)	0·30(3)	0·02(1)	0·01(1)	0·04(2)	0·10(7)	n.d.	101·3	Fo_{86}
19-2	gl(10)	51·2(1)	0·86 (2)	15·0(9)	7·66(14)	0·17(5)	7·98(8)	12·5(1)	2·32(5)	1·77(4)	0·05(4)	0·01(1)	n.d.	94·5	
19-3	gl(6)	51·3(4)	0·93(5)	17·5(2)	8·61(37)	0·10(6)	5·17(8)	9·77(25)	3·08(16)	2·68(9)	0·02(4)	0·08(6)	0·80(7)	95·0	
	cpx(2)	50·4(7)	0·72(2)	8·01(260)	7·00(21)	0·11(4)	13·0(24)	19·4(20)	0·78(39)	0·55(54)	0·13(15)	0·05(6)	n.d.	100·3	$En_{42}Wo_{45}$
	ol(4)	39·5(8)	0·01(2)	0·18(10)	17·1(5)	0·39(18)	43·4(6)	0·38(3)	0·07(5)	0·01(1)	0·01(2)	0·17(14)	n.d.	101·5	Fo_{82}
19-4	gl(9)	51·3(2)	0·85(2)	15·4(1)	7·63(25)	0·17(7)	7·52(9)	12·3(1)	2·40(8)	1·85(4)	0·04(3)	0·03(4)	n.d.	95·0	

	cpx(5)	51·1(9)	0·48(12)	4·32(101)	4·74 (44)	0·10 (8)	15·6(8)	22·5(7)	0·30(10)	0·08(5)	0·52(21)	0·05(5)	n.d.	99·9	$En_{46}Wo_{48}$
9-1	gl(17)	50·8(5)	0·87(5)	16·2(3)	7·78(26)	0·20(7)	6·81(9)	12·2(1)	2·40(11)	1·99(6)	0·05(4)	0·04(8)	0·69(3)	93·6	
	cpx(4)	51·0(11)	0·37(3)	2·93(62)	4·15(27)	0·14(6)	16·2(3)	23·1(3)	0·19(5)	0·03(4)	0·44(16)	0·07(8)	n.d.	98·7	$En_{47}Wo_{49}$
	ol(4)	40·0(3)	0·03(4)	0·02(4)	12·1(4)	0·22(10)	46·0(4)	0·35(5)	0·02(2)	0·02(2)	0·04(4)	0·02(4)	n.d.	98·80	Fo_{87}
18-1	gl(10)	53·0(2)	1·09(3)	17·1(2)	8·14(19)	0·18(6)	5·06(7)	9·72(9)	3·09(4)	2·63(3)	0·03(3)	0·02(2)	n.d.	96·6	
	cpx(6)	49·8(6)	0·69(22)	4·94(108)	6·30(88)	0·19(8)	15·0(8)	21·5(8)	0·37(12)	0·15(13)	0·17(15)	0·07(15)	n.d.	99·1	$En_{45}Wo_{47}$
	ol(5)	40·6(9)	0·04(2)	0·24(31)	16·0(7)	0·30(11)	44·0(10)	0·43(8)	0·02(3)	0·01(1)	0·07(30)	0·03(8)	n.d.	101·8	Fo_{83}
	plag(4)	48·3(3)	0·17(3)	30·1(3)	1·45(25)	0·03(5)	0·72(6)	15·8(2)	1·99(10)	0·49(6)	0·01(2)	0·07(6)	n.d.	99·2	$An_{79}Or_{3}$
12-3	gl(9)	52·6(3)	1·07(8)	17·0(2)	7·89(21)	0·14(4)	5·03(9)	10·1(3)	2·87(7)	2·39(13)	0·01(1)	0·03(6)	0·88(11)	97·0	
	cpx(7)	49·5(8)	0·65(11)	5·04(175)	6·51(53)	0·13(6)	14·6(8)	20·9(6)	0·35(20)	0·15(17)	0·12(5)	0·06(7)	n.d.	98·1	$En_{44}Wo_{45}$
	ol(6)	39·5(5)	0·05(4)	0·04(4)	15·3(4)	0·26(7)	42·6(5)	0·44(9)	0·02(2)	0·02(2)	0·02(3)	0·02(4)	n.d.	98·2	Fo_{83}
	plag(3)	47·1(3)	0·02(2)	30·6(5)	0·91(21)	0·02(4)	0·42(13)	16·6(5)	1·91(5)	0·23(6)	0·05(5)	0·02(3)	0·18(5)	98·1	$An_{82}Or_{1}$
12-2	gl(10)	53·2(3)	1·18(5)	16·5(2)	8·05(19)	0·20(10)	4·38(20)	8·99(21)	3·15(11)	3·31(8)	0·03(5)	0·10(9)	0·95(10)	96·0	
	cpx(7)	50·5(4)	0·77(10)	6·38(110)	6·87(53)	0·12(8)	13·8(10)	19·9 (11)	0·56(18)	0·40(28)	0·04(4)	0·05(11)	0·35(8)	99·7	$En_{43}Wo_{45}$
	ol(3)	38·8(2)	0·06(5)	0·06(6)	17·7(1)	0·34(13)	40·6(2)	0·41(12)	0·02(3)	0·02(2)	0·01(1)	0·05(6)	0·32(2)	98·4	Fo_{80}
	plag(1)	49·2	0·31	27·0	1·54	0·00	1·72	15·5	2·44	0·58	0·03	0·07	0·31	98·73	$An_{75}Or_{3}$
12-1	gl(11)	52·3(3)	1·17(13)	17·4(7)	7·95(41)	0·21(16)	4·14(24)	9·66(43)	3·05(9)	3·06(32)	0·05(8)	0·00(0)	0·97(3)	95·3	
	cpx(3)	49·3(5)	0·76(22)	8·52(76)	6·62(107)	0·23(12)	12·4(4)	19·2(4)	0·76(5)	0·56(23)	0·10(11)	0·03(3)	0·34(14)	98·8	$En_{42}Wo_{46}$
	ol(2)	39·5(5)	0·00(0)	0·22(10)	18·0(3)	0·38(1)	39·4(6)	0·63(25)	0·04(6)	0·03(0)	0·00(0)	0·10(8)	n.d.	98·3	Fo_{80}
	plag(1)	49·7	0·19	25·3	1·68	0·00	1·64	14·1	2·85	0·60	0·00	0·00	0·28	96·3	$An_{71}Or_{4}$

[1]Glass analyses normalized to 100% anhydrous, with all Fe as FeO. Unnormalized total is reported.

[2]Number of microprobe analyses.

[3]One standard deviation in terms of least unit cited.

gl, glass; cpx, clinopyroxene; ol, olivine; plag, plagioclase; n.d., not determined. En = 100 x at. Mg/(Mg + Fe + Ca); Wo = 100 x at. Ca/(Mg + Fe + Ca) in pyroxene, calculated with Fe = FeO; Fo = 100 x at. Mg/(Mg + Fe) in olivine, calculated with Fe = FeO_t; An = 100 x at. Ca/(Ca + Na + K); Or = 100 x at. K/(Ca + Na + K) in plagioclase. PST-9 glass is from Table 1.